

Hull, A. J., Chaston, C. C., Frey, H. U., Fillingim, M. O., Goldstein, M. L., Bonnell, J. W., and Mozer, F. S. (2016), The “Alfvénic surge” at substorm onset/expansion and the formation of “Inverted Vs”: Cluster and IMAGE observations, *J. Geophys. Res. Space Physics*, 121, 3978–4004, doi:10.1002/2015JA022000.

<https://doi.org/10.1002/2015JA022000>

Access to this work was provided by the University of Maryland, Baltimore County (UMBC) ScholarWorks@UMBC digital repository on the Maryland Shared Open Access (MD-SOAR) platform.

Please provide feedback

Please support the ScholarWorks@UMBC repository by emailing scholarworks-group@umbc.edu and telling us what having access to this work means to you and why it’s important to you. Thank you.

RESEARCH ARTICLE

10.1002/2015JA022000

Key Points:

- PBIs are intrinsic part of substorm response to injection and wave energy input from magnetotail
- Injection leads to current breakup to dispersive Alfvén waves and enhanced inverted-V acceleration
- Alfvénic variations dissipate to form inverted-V current during poleward expansion of injection

Correspondence to:

A. J. Hull,
ahull@ssl.berkeley.edu

Citation:

Hull, A. J., C. C. Chaston, H. U. Frey, M. O. Fillingim, M. L. Goldstein, J. W. Bonnell, and F. S. Mozer (2016), The "Alfvénic surge" at substorm onset/expansion and the formation of "Inverted Vs": Cluster and IMAGE observations, *J. Geophys. Res. Space Physics*, 121, 3978–4004, doi:10.1002/2015JA022000.

Received 5 OCT 2015

Accepted 13 APR 2016

Accepted article online 20 APR 2016

Published online 5 MAY 2016

The "Alfvénic surge" at substorm onset/expansion and the formation of "Inverted Vs": Cluster and IMAGE observations

A. J. Hull¹, C. C. Chaston¹, H. U. Frey¹, M. O. Fillingim¹, M. L. Goldstein², J. W. Bonnell¹, and F. S. Mozer¹
¹Space Sciences Laboratory, University of California, Berkeley, California, USA, ²NASA Goddard Space Flight Center, Greenbelt, Maryland, USA

Abstract From multipoint, in situ observations and imaging, we reveal the injection-powered, Alfvénic nature of auroral acceleration during onset and expansion of a substorm. It is shown how Alfvénic variations over time dissipate to form large-scale, inverted-V structures characteristic of quasistatic aurora. This characterization is made possible through the fortuitous occurrence of a substorm onset and expansion phase on field lines traversed by Cluster in the high-altitude acceleration region. Substorm onset was preceded by the occurrence of multiple poleward boundary intensifications (PBIs) and subsequent development/progression of a streamer toward the growth phase arc indicating that this is of the PBI/streamer-triggered class of substorms. Onset on Cluster is marked by the injection of hot, dense magnetospheric plasma in a region tied to one of the preexisting PBI current systems. This was accompanied by a surge of Alfvénic activity and enhanced inverted-V acceleration, as the PBI current system intensified and striated to dispersive scale Alfvén waves. The growth of Alfvén wave activity was significant (up to a factor of 300 increase in magnetic field power spectral density at frequencies $20 \text{ mHz} \lesssim f \lesssim \text{few hertz}$) and coincided with moderate growth (factor 3–5) in the background PBI current. This sequence is indicative of a cascade process whereby small-scale/dispersive Alfvén waves are generated from large-scale Alfvén waves or current destabilization. It also demonstrates that the initial PBIs and their subsequent evolution are an intrinsic part of the global auroral substorm response to injection and accompanying wave energy input from the magnetotail. Alfvénic activity persisted poleward of the PBI currents composing a broad Alfvén wave-dominated region extending to the polar cap edge. These waves have transverse scales ranging from a few tens of kilometers to below the ion gyroradius and are associated with large electric fields (up to 200 mV/m) and Poynting fluxes (up to 200 mW/m² mapped at ionospheric altitudes). The fluctuations show mixtures of traveling and/or reflected (including standing) wave signatures, depending on frequency and location. A transition from incoming traveling wave to standing wave signatures is also seen near onset. Depending on location, electron distributions show signatures of Alfvén acceleration, inverted-V acceleration, or evidence of both. Poleward expansion of substorm emissions coincided with the poleward expansion of the hot energetic plasma, and the formation of a large-scale inverted-V current system with concurrent attenuation of Alfvénic fluctuations within the Alfvén-dominated region. We suggest that the attenuation is due to a dissipative effect owing to changes in the dispersive properties of these waves via the injection process and/or due to a transient magnetotail source. These findings suggest that in addition to playing active roles in driving substorm aurora, inverted-V and Alfvénic acceleration processes are causally linked.

1. Introduction

Substorms are global reconfigurations of the magnetotail that result in the rapid conversion of magnetic energy into particle energy [Akasofu, 1964]. Substorms are preceded by a growth phase, during which magnetic energy builds up in the tail. This energy is suddenly released during a substorm, as the tail relaxes to a stable configuration. The sequence of events that occur during this rapid release of energy has been an area of active research over the past few decades, and to date the mechanisms are not fully understood, prompting considerable debate. Two favored models in the literature that attempt to explain substorm onset are the near-Earth neutral line (NENL) model [e.g., Baker et al., 1996; Shiokawa et al., 1997] and the current disruption (CD) model [e.g., Lui, 1991; Roux et al., 1991]. In the NENL model substorms are first triggered by reconnection

in a near-Earth neutral line in the midtail region (at $\sim 20\text{--}30 R_E$). The resulting burst of fast plasma flow propagates inward and eventually slows down during its encounter with a high pressure plasma on more dipolar magnetic field lines closer to Earth. The braking and diversion of the flow and associated enhancement of magnetic shear in the inner magnetosphere set up the currents that drive substorm current wedge development. This process ultimately results in a sudden brightening (auroral onset) on or near the equatorwardmost discrete auroral arc. The reconnection site later moves tailward to the distant tail region. In the current disruption model a localized instability mechanism occurring inside $\sim 10 R_E$ interrupts and diverts the cross-tail current into the ionosphere via field-aligned currents leading to auroral substorm onset. This is followed by activity that propagates progressively outward and ultimately induces reconnection in the midtail region.

Recent observations are providing important new insight into substorms and suggest either that revisions or alternative paradigms need to be considered. The studies by Angelopoulos *et al.* [2008, 2009] reported observations of substorms that are initiated by reconnection, followed by onset, and then current disruption. This sequence of events cannot fully be explained by the NENL or the CD model. Other studies based on emission data [e.g., Kepko *et al.*, 2009; Nishimura *et al.*, 2010; Mende *et al.*, 2011] indicate that poleward boundary intensifications (PBIs), or more precisely auroral streamers, are an important trigger of many substorms. Owing to established observational connections between PBIs and bursty bulk flows, such events present evidence of substorms initiated by reconnection processes. However, a significant number of substorms do not show this pattern and proceed independently of PBI activity. Moreover, other recent studies reported evidence of substorms initiated by processes in the near-Earth tail [e.g., Rae *et al.*, 2009, 2010; Liang *et al.*, 2008; Lui *et al.*, 2008; Hwang *et al.*, 2014; Murphy *et al.*, 2014]. In a case study based on all-sky images and ground-based magnetometer data, Rae *et al.* [2010] found that the temporal variations and spatial scales of auroral forms are not consistent with a NENL-like mechanism but are most consistent with the cross-field current instability or a ballooning instability triggered close to the inner edge of the ion plasma sheet. They did not see any evidence of a PBI-initiated onset. The results of this study were also found to be consistent with the near-geophysical onset model (a variation of the current disruption model that incorporates important magnetosphere-ionosphere coupling effects attributed to Alfvén waves in the substorm development process) [e.g., Maynard *et al.*, 1996a, 1996b; Erickson *et al.*, 2000]. Building on the results of Rae *et al.* [2010], the statistical study by Kalmoni *et al.* [2015] of auroral bead initiated substorm events indicated that these are most likely due to the shear flow ballooning instability. The study by Murphy *et al.* [2014] reported substorm events consistent with being initiated by an instability in the inner magnetosphere with no apparent precursor reconnection signatures or evidence of auroral streamers. A secondary substorm activation with NENL evolutionary characteristics was also shown to occur during the expansion phase of a substorm attributed to the current disruption/plasma instability mechanism. These results suggest that either or both types of substorm-triggering processes can take place during a substorm active period depending on conditions, explaining and adding to the interpretive complexity of the substorm process. The study by Hwang *et al.* [2014] reported observations from Cluster of tailward propagating near-Earth current disruption signatures followed by signatures of reconnection, which later resulted in a strong substorm enhancement (as inferred from conjunctive ground magnetometer data). In short, these recent studies show that substorms may have different triggering mechanisms and hence sequences of events, which to date are not fully understood.

The auroral acceleration region is an integral link in the chain of events that transpire during substorms, and the currents, plasma, and electric fields undergo significant changes driven by complex dynamical processes deep in the magnetotail. Acceleration processes that occur therein energize and heat the plasma that ultimately leads to some of the most intense global substorm auroral displays. Though this region has garnered considerable attention, the time evolution of field-aligned currents, associated acceleration processes, and resultant changes in the plasma that occur during key stages of substorm development remain unclear. The study of evolutionary sequences in the acceleration region is important because it provides key insight into how substorms form and evolve, such as the structure of the field-aligned currents that form, what acceleration processes are involved, the nature of momentum and energy flow/conversion that transpire, and consequences of these processes to the plasma and aurora.

Regions of interest for auroral acceleration processes generally can be organized into three broad categories: (1) the upward current region, (2) the downward current region, and (3) the Alfvén region. In the upward current region upward directed parallel electric fields map to convergent perpendicular fields at higher altitudes yielding a “U-shaped” potential configuration. “S-shaped” configurations have also been commonly

inferred [e.g., Mozer *et al.*, 1980] and are associated with a monopolar perpendicular field. In these configurations electrons are accelerated toward and ions away from Earth by “quasistatic” parallel electric fields. Here quasistatic is taken to mean that the potential configuration is invariant over a particle transit time. The upward current acceleration region may extend down to altitudes (above Earth’s surface) as low as a few thousand kilometers at its lower boundary and extend up to $\sim 5 R_E$ altitudes at its upper edge; however, a significant fraction (up to 50%) of the parallel potential drop nominally occurs between $0.5 - 1.0 R_E$ and $2.0 - 2.5 R_E$ altitude ranges [e.g., Mozer and Hull, 2001; Paschmann *et al.*, 2003; Li *et al.*, 2014; Alm *et al.*, 2015, and reference therein]. At low altitudes, the electron precipitation signatures are characterized by relatively sharp monoenergetic peaks. Because they often have an inverted-V shape in spectrograms, these electrons were termed inverted-V events. A similar quasistatic U-shaped potential paradigm is often used to describe downward current regions. However, in this case downward directed parallel electric fields map to higher-altitude diverging electric fields and is of a sense to accelerate electrons away from and ions toward Earth. The Alfvén region, generally viewed as separate from the other regions, is highly dynamic and is characterized by variable Alfvén wave electric and magnetic fields, and field-aligned electrons that have been accelerated over a broad energy range. The resulting precipitation leads to so called “Alfvén” aurora, which are dynamic and, under quiet conditions, are weak emission signatures. However, during more active times, Alfvén wave activity is much more intense at the plasma sheet boundary layer and can power some of the most intense auroras near midnight [Wygant *et al.*, 2000; Keiling *et al.*, 2002, 2003].

Resolving the complex interrelated processes that occur during substorms requires multipoint observations at key locations within the acceleration region to better establish the spatial morphology of attendant plasma and fields as they evolve in time. Such a capability is enabled by the Cluster mission, which to this date has sampled much of the auroral acceleration region with four closely spaced probes during perigee passes. Earlier in the mission, Cluster perigee passes transected the high-altitude acceleration region (~ 3.0 to $5.0 R_E$ altitudes), while during more recent times these were well within the acceleration region. A growing number of studies based on multipoint data from Cluster are beginning to unravel the structure and dynamics of the upper end [e.g., Marklund *et al.*, 2001; Kistler *et al.*, 2002; Marklund *et al.*, 2004; Aikio *et al.*, 2004, 2008; Hull *et al.*, 2010; Alm *et al.*, 2015] and deep within the heart of the auroral acceleration region [e.g., Marklund *et al.*, 2011a, 2011b, 2012; Forsyth and Fazakerley, 2012; Forsyth *et al.*, 2014]. However, as far as we know, there are few multipoint studies that address the formation of field-aligned currents, associated acceleration processes, and effects on plasma constituents that occur during initial stages of substorm development (near onset and expansion phase) within the auroral acceleration zone. Kistler *et al.* [2002] reported on the velocity, and the spatial and temporal coherence of ion outflow observed in the nightside auroral region during a substorm. They found that ion outflow structures were spatially coherent over 3–4 min time scales and were moving at the convection velocity. Higher energy outflow were found to be collocated with enhanced auroral emission signatures. The recent study by Forsyth *et al.* [2014] focused on the detailed azimuthal structure of the substorm current wedge sampled by two Cluster spacecraft during an approximate longitudinal (east-to-west) transect of the auroral acceleration region. They found that the gross macroscale features of upward and downward field-aligned currents associated with the wedge current were superposed with a nested series of oppositely directed, smaller-scale, north-south aligned current sheets. The presence of these small-scale current sheets shows that the substorm current wedge is more complex than the often presumed simplified paradigm of a single loop of a downward magnetic field-aligned line current into the ionosphere at the eastern edge of the bulge connected to an upward line current at the western edge via a westward ionospheric line current and an eastward magnetospheric current. Marklund *et al.* [2012] addressed the structure of the acceleration region potential and currents associated with the westward surge and connected horn of an auroral substorm. Marklund *et al.* [2011b] studied the development of quasistatic arcs and interaction with Alfvénic processes at the polar cap boundary region during the recovery phase of a substorm. The results show that Alfvénic and quasistatic acceleration are both active in this region, transitioning from being equally important to being predominantly quasistatic. A sudden expansion of the plasma sheet boundary layer (PSBL) as observed by Cluster during the recovery phase of a substorm is documented by Aikio *et al.* [2008]. This expanded PSBL was characterized by a nested series of equatorward drifting upward and downward currents embedded in a large-scale downward current region. These small-scale currents had features in electrons characteristic of broadband acceleration. Although occurring during quiet magnetospheric conditions, Hull *et al.* [2010] presented Cluster observations at key instances during the formation of a new quasistatic up-down current system, which led to a PBI. The results suggest a possible linkage between

the Alfvén region and quasistatic arc current systems never before realized by single spacecraft. Namely, they suggest that quasistatic systems of field-aligned currents are born out of the highly dynamic Alfvénic region at the plasma sheet boundary layer and that the Alfvénic region may be the initial stage in the development of quasistatic systems. Magnetometer data from the low-altitude multispacecraft mission AMPERE are also providing new insight on the two-dimensional morphology and evolution of substorm current systems. Particularly, *Murphy et al.* [2013] demonstrated that the nightside field-aligned currents are significantly reduced or disappear several minutes just prior to substorm onset. Though consistent when averaged, they also showed that the gross structure of the substorm current wedge observed during the expansion phase is more complex than the standard line current wedge paradigm.

Here we utilize the unique multipoint capabilities of Cluster in combination with global auroral images from IMAGE to analyze the plasma and field properties within the high-altitude acceleration region ($4.4 R_E$ geocentric distance) during the onset and expansion phase of a substorm. The Cluster fleet was appropriately spaced in a “string-of-pearls” configuration when it made a latitudinal transect of the plasma sheet near midnight, magnetically conjugate to the center-east part of the developing substorm auroral bulge. This event is quite remarkable in that Cluster captured key elements of current, plasma, and potential temporal development, particularly the following: (1) a surge in intense Alfvénic activity associated with the intensification, and breakup of a preexisting PBI current system near initial onset, and (2) the growth of a large-scale inverted-V arc system out of a region dominated by Alfvénic acceleration processes, associated with expansion of substorm auroral emissions. It is the primary purpose of this paper to report on the results of a detailed analysis of these temporal sequences with the aim of providing a better understanding of how the substorm-related current systems, associated plasma, and potentials form and evolve. As there are few multispacecraft observations of such processes, it is also the intent of this paper to provide a useful observational basis for comparison with theoretical models and other multispacecraft observations of substorm-related processes. The paper is organized in the following manner. Section 2 describes the Cluster and IMAGE instrumentation and data sets used. A detailed presentation of the plasma and field observations that characterize the substorm event is given in section 3. Here we highlight the sequence of events that transpire in the high-altitude plasma sheet during the initial onset and expansion phase of a substorm. Particular attention is placed on the geometry, structure, and motion of the currents, the development of the parallel potential drops, electric fields, and Alfvénic Poynting flux, and the reorganization of the plasma that occur. We also explore interrelationships between the electric and magnetic fields, including E - B ratios, coherence, and phase response. By examining these properties, we are able to diagnose how the injection process affects the nature and relative importance of inverted-V and Alfvénic acceleration processes that occur in this region. The discussion and the summary and conclusions are given in sections 4 and 5.

2. Instrumentation and Experimental Data Set

In situ observations in the high-altitude acceleration region are from the Cluster mission. Electron data were sampled by the Plasma Electron and Current Experiment (PEACE) [Johnstone et al., 1997], which is composed of two sensors mounted on opposite sides of each spacecraft, the Low-Energy Electron Analyzer (LEEA) and a High-Energy Electron Analyzer (HEEA). Typically, electrons are measured by PEACE-LEEA in the energy range from 0.7 eV to 1 keV, and by PEACE-HEEA from 30 eV to 26 keV. It is important to note that LEEA and HEEA sample velocity space half a spin (2 s) out of phase. While the overlapping data from the two sensors are usually in good agreement, significant differences do occur and are generally attributable to aliasing in short-scale space and/or time variations. Ion data are provided by the Cluster Ion Spectrometry (CIS) experiment [Réme et al., 1997]. CIS is composed of two instruments, a Hot Ion Analyzer (HIA) and a time-of-flight ion COMposition and Distribution Function (CODIF) analyzer, which measures the major ions in the range 5 eV q^{-1} – 40 keV q^{-1} . In this event ion measurements from HIA are only available on two of the spacecraft (SC1 and SC3), and data from CODIF are only available on three of the spacecraft (SC1, SC3, and SC4). We used data from the Electric Field and Wave (EFW) experiment [Gustafsson et al., 1997], which measures the spin plane components of the electric fields at 25 samples per second. We also used magnetic field data at 22 samples per second from the Fluxgate Magnetometer (FGM) experiment [Balogh et al., 1997].

To provide global auroral context for the in situ observations, data from the Wideband Imaging Camera (WIC) of the far ultraviolet (FUV) instrument on board IMAGE is also presented [Mende et al., 2000]. The FUV-WIC instrument is sensitive to the spectral range from 140 to 160 nm and provides images (20 s integration time) every 2 min.

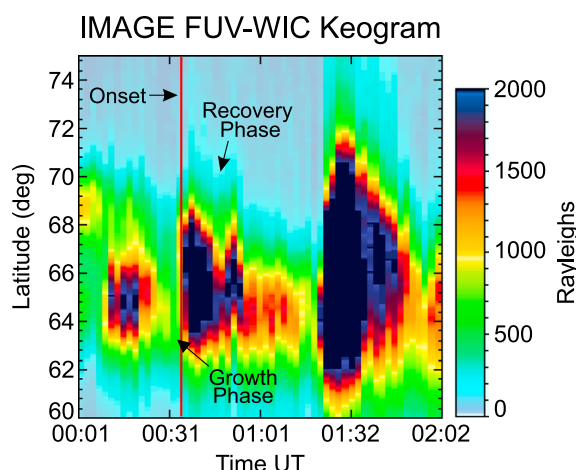


Figure 1. Keogram of auroral emissions sampled near midnight (0.0 ± 0.5 h MLT) by IMAGE-WIC.

3. Observations

3.1. Time Sequence Overview

On 26 February 2001 from 0034 UT to 0048 UT the Cluster fleet made a poleward pass of the Northern Hemisphere auroral acceleration region near midnight during which a substorm occurred. Observations from the Wind spacecraft in the solar wind show that the interplanetary magnetic field was southward with $B_z \sim -4$ nT, the solar wind velocity was ~ 290 km/s, and the density was ~ 8 cm $^{-3}$ during the event (data not shown). The substorm was one of a quasiperiodic series of substorm activations of increasing strength that occurred during the first couple hours on this day as shown by the keogram of emissions from the IMAGE FUV-WIC given in Figure 1. The substorm growth phase, which follows the recovery phase of the previous brightening, is evident by the equatorward drift of relatively weak auroral emissions prior to substorm onset indicated by the red line in Figure 1. The expansion phase was relatively short, lasting $8 \text{ min} \pm 1 \text{ min}$. Recovery phase begins ~ 0045 UT and is indicated by the characteristic slow dimming and contraction of auroral emissions to lower invariant latitudes that lasts ~ 30 min.

A complimentary view of auroral emissions is given in Figure 2, which shows a series of global images in magnetic apex coordinates from IMAGE-WIC during the substorm. The ionospheric foot points of each Cluster spacecraft are indicated by the blue crosses in each panel. The images shown in Figures 2a and 2b were sampled during the growth phase. The auroral emissions were more or less stable with similar signatures observed in both images. Near midnight, the growth phase arc is centered at a magnetic latitude of $\Lambda \sim 64^\circ$, which is equatorward from the open-closed field boundary indicated by the termination of weak emissions that occur at higher latitudes. In the following image (Figure 2c) multiple emission intensifications suddenly appear (at $\Lambda \sim 67^\circ - 68^\circ$) in the vicinity of the poleward edge of the auroral oval (indicated by the arrows), one of which is in the vicinity of the Cluster foot points. Their poleward location indicates that these are poleward boundary intensifications (PBIs). There does appear to be evidence of faint bridges extending from the PBIs to the growth phase arc. In Figure 2d we see a significant brightening of the middle PBI, which has moved equatorward (0.8° based on emission cuts centered at magnetic local time (MLT) = 0 h) and now appears as an intensified auroral form inclined 35° from the noon-midnight meridian. This feature appeared in the previous image but was much fainter (indicated by cyan line). Accompanying this brightening, evidence of westward, eastward, and poleward expansion of intensified emissions is apparent. This sequence of events suggests that substorm onset occurs near midnight at some time between 0034:21 UT and 0036:24 UT. Though the substorm is developing, the PBI in the vicinity of Cluster's foot points is still apparent in Figure 2d, but it has now moved equatorward over the foot points with no significant change in intensity. In subsequent images the substorm auroral emissions continue to brighten and expand. The most intense brightenings are associated with the equatorward progression and evolution of the PBIs. This is evident in the middle PBI, which intensified as it transitioned to a north-south aligned streamer in Figure 2e. A localized brightening is also seen in the vicinity of the Cluster foot points (near C4 in Figure 2e), as the substorm auroral bulge expanded farther eastward. The data indicate that this is associated with the equatorward progression of the rightmost PBI

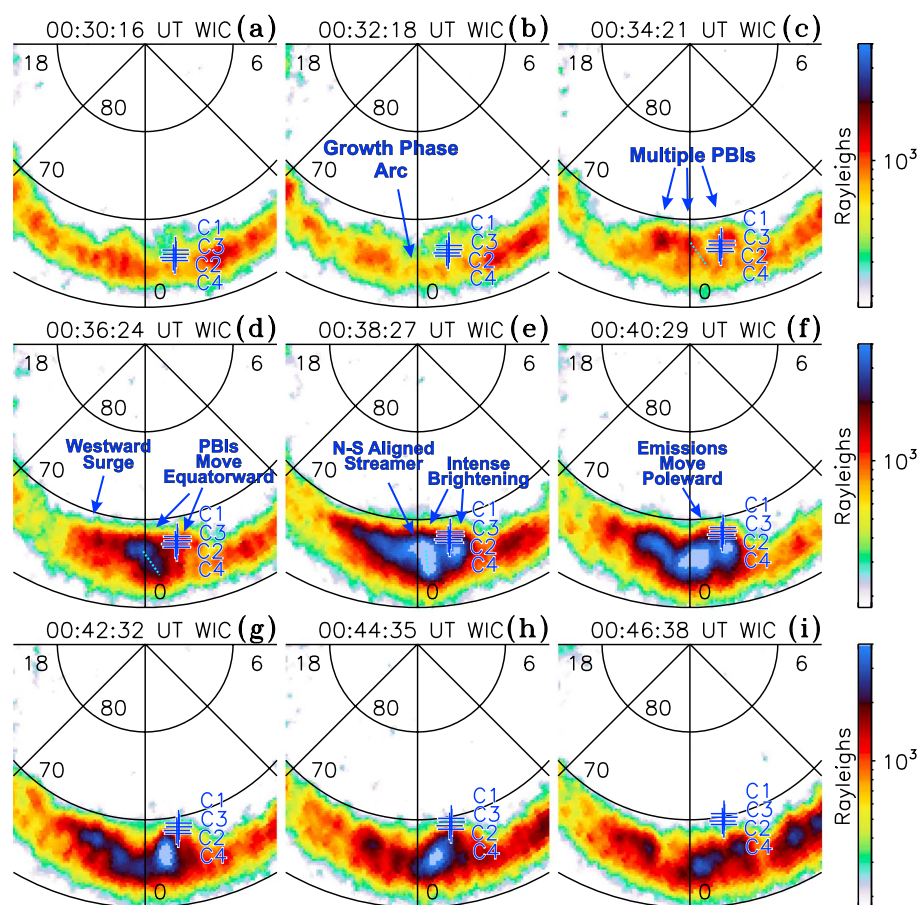


Figure 2. Sequence of auroral images from IMAGE-WIC during substorm. The foot points of each Cluster spacecraft are indicated by the blue crosses and identifying label.

toward the growth phase arc location. The intensified emissions expand poleward toward the lead spacecraft foot point (C1), before the recovery phase begins, during which time Cluster eventually enters into the polar cap (Figure 2i).

The multiple azimuthally distributed intensifications that occur near midnight prior to onset (see Figure 2c) in a way are similar in appearance to auroral beads, also referred to as azimuthal auroral forms or spatially periodic auroral spots, reported in the literature [e.g., *Elphinstone et al.*, 1995; *Liang et al.*, 2008; *Henderson*, 2009; *Rae et al.*, 2009; *Kalmoni et al.*, 2015]. However, their initial occurrence at the poleward edge of the auroral oval and their subsequent equatorward propagation suggest that the intensifications reported here are consistent with the properties of equatorward propagating PBIs, as opposed to auroral beads. The latter appear just prior to breakup as multiple azimuthally spaced intensifications along/on top of the onset arc, which lies well beyond the open-closed field boundary in the vicinity of the equatorward edge of the auroral oval. These are often observed to propagate along the onset arc as they form and evolve and also observed to expand and/or move polewards [e.g., *Henderson*, 2009; *Kalmoni et al.*, 2015]. On the other hand, PBIs refer to localized activations/intensifications in the nightside that occur in the vicinity of the open and closed field boundary, which in auroral emission data corresponds to the poleward edge of the auroral oval. These activations may be preferentially east-west aligned, north-south aligned (denominated as streamers), or inclined somewhere in between [e.g., *Zesta et al.*, 2002]. Multiple PBIs (or streamers) can and have been reported to occur simultaneously at the poleward boundary of the auroral oval during substorm active times [e.g., *Henderson*, 2012; *Lyons et al.*, 2012]. Finally, though the mechanism/role is under considerable recent debate, the fact that the gross expansion of auroral emissions followed the brightening and subsequent equatorward extension of a PBI indicates that this event is of the PBI-triggered class of substorm reported in the literature [e.g., *Kepko et al.*, 2009; *Nishimura et al.*, 2010; *Mende et al.*, 2011].

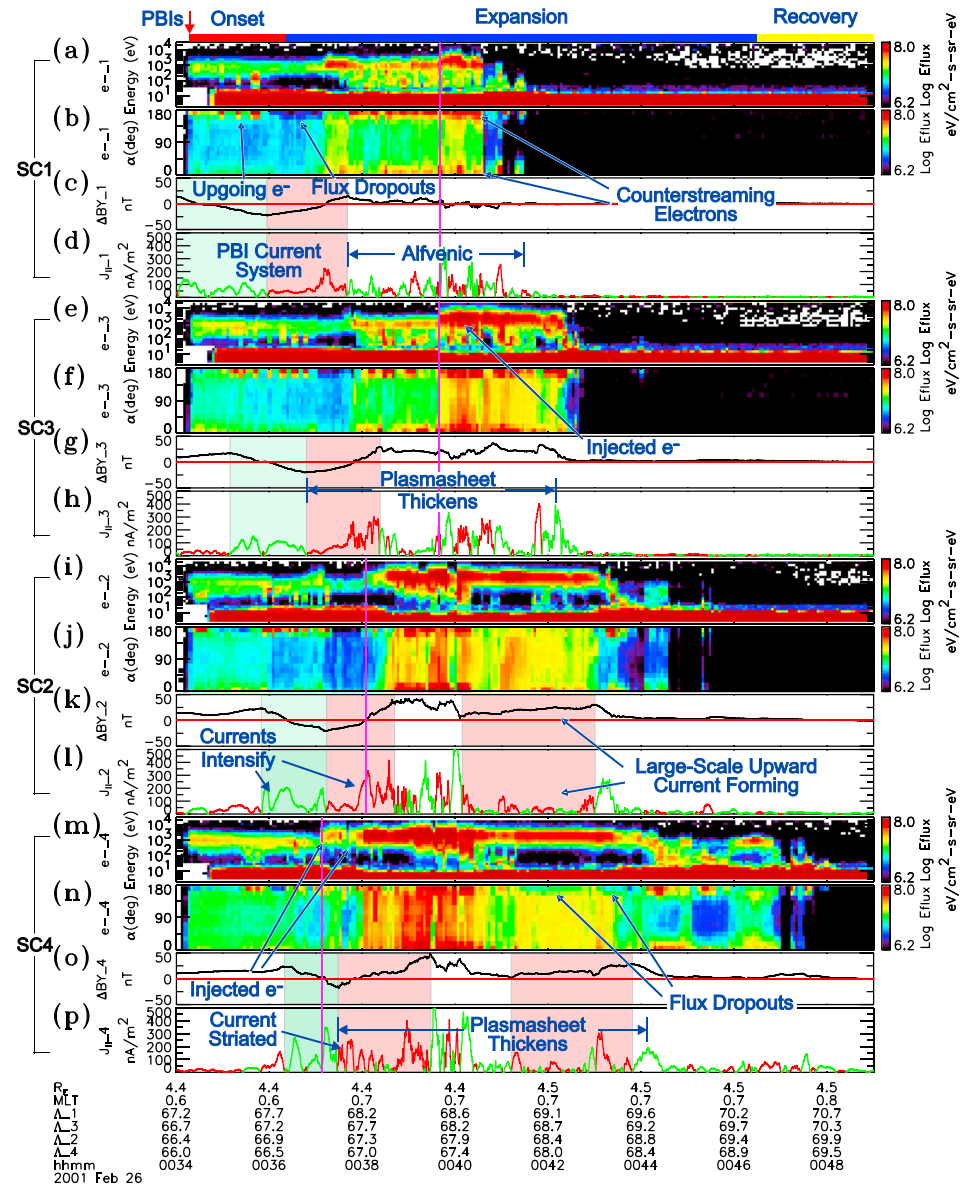


Figure 3. Spectrograms of electron differential energy flux versus (a, e, i, and m) energy and (b, f, j, and n) pitch angle, (c, g, k, and o) the westward component of the perturbation magnetic field ΔB_y , and (d, h, l, and p) estimates of the field-aligned current density $J_{||}$ for SC1 (Figures 3a–3d), SC3 (Figures 3e–3h), SC2 (Figures 3i–3l), and SC4 (Figures 3m–3p).

Cluster was within the high-altitude acceleration region at a geocentric distance of $\sim 4.4 R_E$ during the substorm onset and expansion phase. Cluster is roughly in a noon-midnight polar orbit off of perigee, and thus, the trajectory, when mapped to the ionosphere, corresponds to an invariant latitude transect of the center-east part of the substorm auroral bulge, as indicated by the foot points in Figure 2. The tetrahedron is moving at an average velocity of $V_{tet} = 4.8$ km/s (0.284, 0.374, and 0.883) in geocentric solar ecliptic (GSE) coordinates. This translates to ionospheric foot points that are predominantly moving poleward at an average invariant latitude rate of $0.25^\circ/\text{min}$ during the transect. The along-track separation between the lead and trailing spacecraft is roughly 1470 km, while the cross-track separations range from 105 km to 280 km depending on spacecraft pair. This configuration enables us to study the latitudinal structure of the plasma and fields and how these evolve in time.

Figure 3 shows spectrograms of electron differential energy flux versus energy and pitch angle, the westward component of the perturbation magnetic field ΔB_y , and the magnitude of the current density component

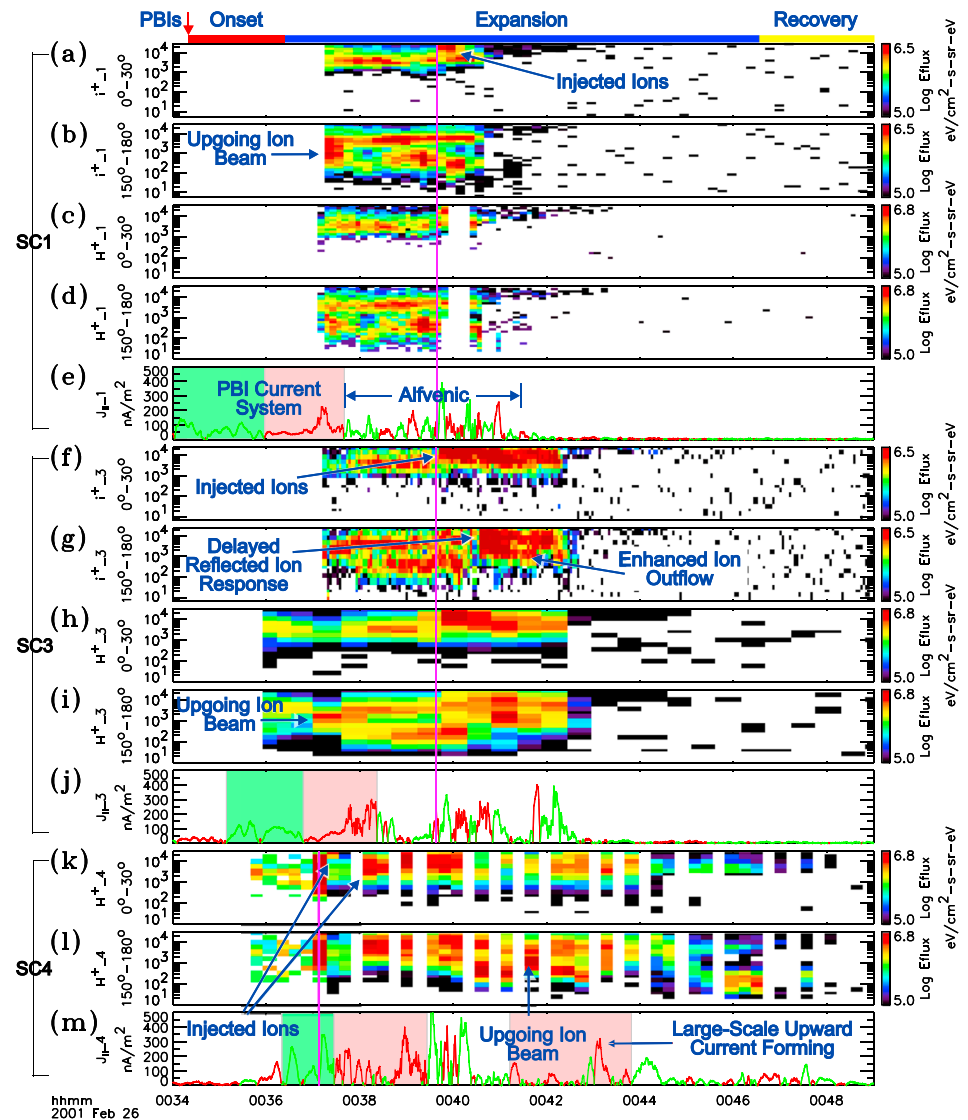


Figure 4. Spectrograms of (a and f) magnetic field-aligned (downgoing) and (b and g) field-opposed (upgoing) ion differential energy flux from HIA, spectrograms of (c, h, and k) field-aligned and (d, i, and l) field-opposed H^+ differential energy flux from CODIF, and (e, j, and m) the magnitude of the field-aligned current density from SC1 (Figures 4a–4e), SC3 (Figures 4f–4j), and SC4 (Figures 4k–4m).

that is parallel to the background magnetic field J_{\parallel} estimated from ΔB_y for all four of the Cluster spacecraft. Upward (downward) current regions are indicated by the positive (negative) slope in the ΔB_y traces, which also correspond to values for J_{\parallel} highlighted in red (green) in Figure 3. Prior to computing J_{\parallel} , values for ΔB_y were smoothed to remove fluctuations with periods shorter than $\lesssim 8$ s. This choice of averaging window was found to provide the best compromise between the desire to show large spatial scale variations with some of the embedded substructure highlighted in this section. Characterization of higher frequency fluctuations removed from the smoothing is reserved for later sections. In Figure 3 the data are displayed in the order each spacecraft crosses the same invariant latitudinal region, with SC1 being first, followed by SC3, SC2, and SC4. Spacecraft SC3, SC2, and SC4 trail SC1 by roughly 1.8 min, 3.2 min, and 4.8 min, respectively.

Ion data sampled by SC1, SC3, and SC4 over the same time interval are shown in Figure 4 in a similar time-ordered sequence. Because of data gaps and different sampling rates, data from both HIA and CODIF are shown. Energy-time spectrograms of magnetic field-aligned (downgoing) and field-opposed (upgoing) ion (i^+) differential energy flux from HIA are only shown for SC1 and SC3. Also shown are downgoing and upgoing

proton (H^+) energy flux spectrograms from CODIF for SC1, SC3, and SC4. Current densities are also included as a visual reference.

Based on the foot points of Cluster on the auroral images, the time interval of data depicted in Figures 3 and 4 encompasses the plasma sheet region that maps to the poleward part of the auroral oval, as well as the initial entry into polar cap region. This interval of data optimally spans the initial onset, expansion, and early recovery phase of the substorm. Approximate times of the substorm phases inferred from the auroral images are indicated by the color-coded bar at the top of Figures 3 and 4. The time when multiple PBIs first occurred is also indicated by the red arrow. The estimated times have an uncertainty of ± 1 min, given that the auroral images have a 20 s time resolution given every 2 min.

According to the images, substorm onset occurs at some time between 0034:21 UT and 0036:24 UT (red bar at top of figure). During this interval the lead spacecraft SC1 is traversing a large-scale current pair system (a downward current region shaded in green followed by an upward current region shaded in red in the interval from 0034:00 UT to 0037:40 UT in Figure 3d). The auroral images sampled during this period indicate that Cluster is traversing field lines connected to the rightmost PBI in Figures 2c and 2d. Note that the upward current part was encountered nearly 2 min after the initial occurrence in the auroral image in Figure 2c, as the PBI progressed equatorward to lower latitude over the Cluster foot points. The magnitude of the downward field-aligned current density is on average ~ 60 nA/m², which maps to a value of 5100 nA/m² at ionospheric altitudes, assuming a dipole magnetic field model and J_{\parallel}/B is constant. Similarly, the upward field-aligned current density is typically 50 nA/m² but attains a peak value of ~ 230 nA/m². These map to ionospheric values of 4300 nA/m² and 20000 nA/m², respectively. The normal to the current pair, determined from a variance analysis applied to the perturbation magnetic field, is oriented within $\sim 10^\circ$ of the magnetic meridional plane and perpendicular to the background magnetic field. This indicates that the system is preferentially aligned in the east-west direction. Moreover, the separation of the eigenvalues (maximum to intermediate value ratio ~ 10) indicates that the system is well described as a pair of field-aligned sheets of current. The integrated intensities of the downward and upward current parts are found to be balanced (to within 0.4%) with values estimated at -27.3 mA/m and 27.2 mA/m, respectively. This suggests that the PBI currents are locally closed in the ionosphere via a meridional (poleward directed) current.

No apparent sign of substorm activity is manifested in the electrons and ions sampled by SC1 in this interval. The plasma is relatively cold, and tenuous, with the electron and proton temperatures estimated at ~ 360 eV and 1.3 keV, respectively, and the average plasma density being estimated at 0.4 cm⁻³. The electrons and ions in both the upward and downward current parts of the PBI system show signatures that are consistent with acceleration in quasistatic potential drops. For example, electron beams with energies reaching ~ 100 –200 eV are observed throughout the downward current interval (0034:00 UT–0036:00 in Figure 3a). These electron beams are predominantly moving upward along the magnetic field, as indicated by the preferential energy flux enhancements near 180° in the pitch angle spectrogram in Figure 3b. Examples of electron phase space density (top) and differential energy flux (middle) spectra as a function of energy sampled by SC1 in a local downward current region at 0035:40.877 UT are shown in Figure 5a. For clarification purposes, a complimentary view of the electron distribution function in v_{\perp} – v_{\parallel} space is also shown (bottom). This example shows an upgoing electron beam with a peak at ~ 100 –120 eV energy (red enhancement), which is superposed on a hotter, nearly isotropic plasma sheet distribution. Upgoing electron beams are characteristic of acceleration by downward directed parallel electric fields below the spacecraft [e.g., *Marklund et al.*, 1997]. Differences in the upgoing beam signatures from the LEEA and HEEA detectors indicate variability on a half-spin time scale (2 s), which may be spatial and/or temporal. Unfortunately, no ions were measured in this region, so we cannot comment on their properties here.

In contrast, the electron distributions observed in the adjacent upward current region have a preferential downgoing skew. This is due in part to a preferentially downward directed field-aligned beam/peak in distribution function at energies approximately few hundred eV. As an example, Figure 5b shows phase space density (top) and differential energy flux (middle) spectra of electrons sampled by SC1 in an upward current region at 0037:12.998 UT. The broad peak in the distribution function suggests that only a small acceleration potential ($\sim 300 \pm 200$ V) exists above the spacecraft. The distributions also exhibit modified loss cone features with dropouts (or depressed values) near 180° pitch angles (upgoing direction) at energies $\lesssim 1$ keV, which are also clearly visible in the velocity space distribution function shown in the bottom panel and pitch angle spectrogram (interval from 0036:00 UT to 0037:40 UT in Figure 3b). The modified loss cone features are indicative

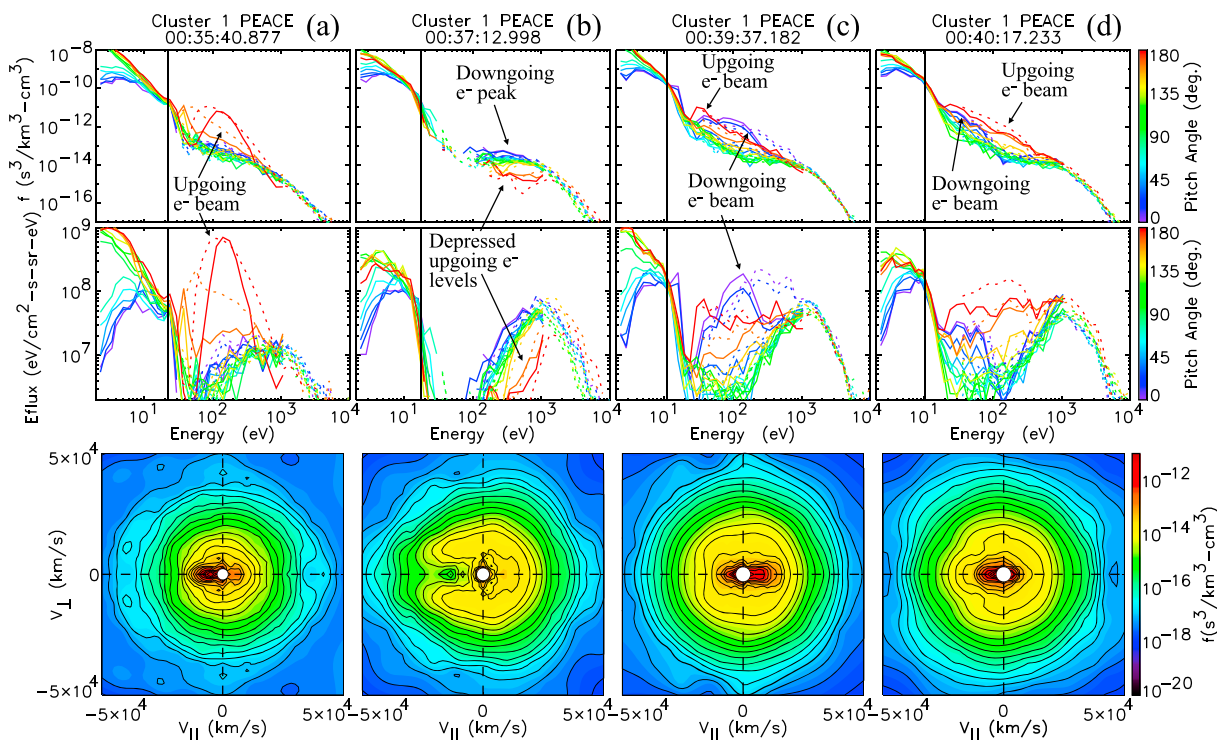


Figure 5. (a–d) (top) Electron distribution function and (middle) differential energy flux spectra as a function of energy for different pitch angles from SC1 sampled at four different locations during its transect of the plasma sheet. Data from LEEA are indicated by the solid curves and HEEA by the dashed curves. Spectra at pitch angles near 0° (purple/blue curves) correspond to downgoing or precipitating electrons, while spectra at pitch angles near 180° (red/orange curves) correspond to upgoing electrons. The solid vertical lines indicate the magnitude of the measured spacecraft potential. (bottom) Also shown are electron distribution functions in velocity space from HEEA. Here $v_{||}$ and v_{\perp} are parallel and perpendicular to the background magnetic field.

of a sizable potential drop below the spacecraft due to upward directed parallel electric fields, which prevents ionospheric photoelectrons and backscatter electrons that have insufficient energy from reaching this altitude [Kletzing and Scudder, 1999]. This results in electron distributions in velocity space that are horseshoe like in appearance as shown in Figure 5b (bottom). Confirming the existence of a potential drop below SC1, these electrons are coincident with upgoing ion beams with energies approaching ~ 1 keV (see Figure 4b). These observed electron and ion signatures are indicative of an inverted-V type of acceleration region that has a total potential drop of ~ 1.3 kV, most of which occurs primarily below the spacecraft.

The current sheet pair system is subsequently sampled by spacecraft SC3 and SC2, although the currents have intensified. As will be demonstrated later in section 3.2, the current pair system is also found to be moving equatorward. The time interval, location relative to the auroral emission signatures, propagation characteristics, and steadiness of the current system demonstrate that the current system is causally connected to the local PBI enhancement that occurs just prior to substorm onset.

Poleward of the PBI current system, SC1 encounters an extended region (~ 0038 UT to ~ 0040 UT in Figures 3c and 3d) of short-scale, variable currents. The currents in this region have peak current density amplitudes ranging from 75 nA/m^2 to 400 nA/m^2 , which map to values ranging from 6400 nA/m^2 to $34,000 \text{ nA/m}^2$ at ionospheric altitudes. Note that temporal variations in the magnetic fields during the local transit time could lead to inaccuracies in the current density computations. However, despite noticeable changes in time, the similarities among sequential spacecraft along with corroboration with electron signatures to be shown below, suggest that the magnetic field variations in this region, for the most part, are sufficiently stable to provide reasonable local estimates of current that have considerable interpretive capability. Nevertheless, the values of the current density should be viewed as approximate. The small-scale currents are alternating between upward and downward current sense at a cadence of $\sim 15 \pm 6$ s, which corresponds to magnetic field fluctuations in the Pi1 pulsation band. The currents have thicknesses ranging from 10 km to nearly 100 km, with a typical width of 60 ± 20 km. These map to thicknesses of 7 ± 3 km at ionospheric altitudes. On SC1 these currents vary from being primarily east-west aligned sheets (0038:30–0039:30) to north-south aligned

sheets (0039:30–0041:00 UT). However, current filaments are also observed. These have near degenerate maximum and intermediate eigenvalues in a variance analysis applied to the magnetic field data (not shown). The ratio of E_{\perp}/B_{\perp} associated with these currents is estimated to be on the order of the local Alfvén speed (6000 km/s), which suggests that these are Alfvén waves. These variable currents are accompanied by magnetic field-aligned electrons that are distributed over a broad energy range (10 eV to 400 eV in Figure 3a). These broadband electrons have a sense relative to the magnetic field that varies between parallel, antiparallel, or counterstreaming (see Figure 3b). Electron distributions in these variable currents are likely aliased. Nevertheless, distributions in upward Alfvénic currents often appear to have enhanced downgoing beam signatures, whereas the distributions in downward Alfvénic currents tend to show strong isolated upgoing beams (or preferential enhancements in the upgoing beam component of counterstreaming electrons). An example of the former case is given in Figure 5c, which shows electron distribution spectra sampled within a localized upward Alfvénic current at ~0039:37 UT. The distributions exhibit counterstreaming electron signatures, with the downgoing component being more energetic. This preferential downgoing component is most apparent in the electron velocity space distribution shown in Figure 5c (bottom). In contrast, the distribution and energy flux spectra sampled ~0040:17 UT in a downward Alfvénic current given in Figure 5d shows counterstreaming electrons with the upgoing component being more intense and extending to higher energies than the downward component. Indeed, there are exceptions related to smaller-scale temporal and/or spatial variations. Ion outflow is also observed at energies on the order of a few hundred of eV. These are likely ion conics that reach this altitude via the transverse acceleration and/or heating below the spacecraft and with the help of the magnetic mirror force. The signatures observed during SC1's transect of the region are characteristic of the Alfvénic acceleration region. The occurrence of this region after the PBI system indicates that the plasma sheet boundary is not contracting to lower latitudes as the PBI currents intrude equatorward into the plasma sheet. On the contrary, these results indicate that new Alfvénic current systems are forming in the wake of the PBI current system during the early expansion phase of the substorm.

The first clear evidence of substorm activity at Cluster's altitude is seen by the trailing spacecraft SC4 and is marked by the sudden appearance of a denser, hotter, and more energetic population of electrons near ~0037:00 UT (indicated by the magenta line in Figure 3m). This energetic component persists up to ~0044:00 UT, subsequent to which the electron energy decreases with increasing latitude, as SC4 begins its entry into the polar cap. However, during this process, SC4 does appear to reenter the plasma sheet near ~0046:00 UT before finally exiting into the polar cap at higher latitude at ~0047:00. (Note that because this reentry is not seen by the other spacecraft, it is unclear whether it is due to tail flapping or the formation of a new system at the PSBL.) This energetic electron population has a density of $\sim 4 \text{ cm}^{-3}$, and the electron temperature is $\sim 1.4 \text{ keV}$. The energetic electrons are observed coincident with injected energetic ions indicated by enhancements in the proton energy fluxes from $\sim 1 \text{ keV}$ up to, and likely beyond, the detector energy limit of $\sim 40 \text{ keV}$ in Figures 4k and 4l. A lower bound estimate of the proton temperature from SC4 is found to be $\sim 5 \text{ keV}$.

The injection occurs in the region tied to the preexisting PBI current system initially traversed by SC1. However, during SC4's transit of the region, the PBI current pair system has undergone dramatic changes. The upward current part has broadened and intensified (red shaded interval from 0037:28 UT–0039:27 UT in Figures 3o and 3p). Interestingly, this coincides with the intense localized brightening of emissions in the vicinity of Cluster spacecraft foot points (near C4 in Figure 2e). The integrated current intensity (not shown) of the upward current interval increased to a value of 45 mA/m, which is noticeably larger than its downward current counterpart estimated at -30 mA/m . Thus, in contrast to the results found during SC1's transect of the region, the PBI current pair system is no longer balanced. The upward current value also represents a relative growth of 65% from the initial upward integrated current intensity observed during SC1's transit of the region. In contrast the downward integrated current intensity only undergoes a small 10% increase from its initial value. The cause of the unbalanced current is unclear. One possibility is that in addition to being closed locally via meridional currents to the adjacent downward current region, the upward current part may be partially nonlocally connected via westward currents in the ionosphere to downward currents elsewhere (e.g., eastward) in the oval. However, another likely explanation is that the currents are not time stationary but are changing (increasing) significantly during the total time the spacecraft took to cross the current pair system.

Additional to the gross intensification, the upward current part is now striated with a nested series of intense, short spatial scale currents over part of the interval (from 0037:28 UT to 0038:40 UT in Figure 3p).

The short-scale currents alternate between upward and downward current sense at a cadence of ~ 7 s with the upward current densities being more intense (~ 150 – 350 nA/m²) than the downward current counterparts ($\lesssim 75$ nA/m²). As will be demonstrated below, this asymmetric pattern is the result of superposed Alfvén wave fluctuations with sufficient intensity to affect the sense of the large-scale background upward current. Owing to the 4 s cadence of the PEACE data, the electrons are coarsely sampled over these variable currents. Nevertheless, close inspection reveals that the electrons have distribution features that vary in concert with the variations in current sense. Namely, there is a general tendency for the upward current regions to be associated with enhancements (or beams) in the precipitating plasma sheet electrons (or counterstreaming electrons), while downward currents are associated with upgoing electron beams. To demonstrate this behavior, an example of the electron distribution sampled in a downward current fluctuation is shown in Figure 6a. An intense field-aligned upgoing electron beam extending up to 1–2 keV energies with little or no downgoing counterpart superposed on a relatively hot plasma sheet population is clearly visible in the distribution spectra, as well as in the velocity space distribution. In contrast, the electron distribution sampled in a nearby upward Alfvénic current region (see Figure 6b) indicates the presence of counterstreaming electron signatures, with a preferential downgoing sense. The preferential precipitating skew is most apparent in the electron velocity space distribution (from HEEA) shown in Figure 6b (bottom). The Alfvénic modulations appear to be reduced in the latter part of the large-scale upward current region (interval from 0038:40 to 0039:27 UT in Figures 3o and 3p). Here the electron distributions show evidence of quasistatic acceleration both above and below the spacecraft, namely, a precipitating beam and modified loss cone features. In some places these distributions are superposed with transient Alfvén acceleration signatures. As an example, Figures 6c and 6d show sequentially sampled electron distribution functions in the vicinity of the current density peak in Figure 3p. Both of these samples show a strong precipitating beam at energies ~ 1.5 – 1.7 keV, suggesting that a sizable inverted-V parallel potential drop exists above the spacecraft. Evidence of flux dropouts in the field-opposed direction at energies $\lesssim 1$ keV is also seen in both samples, suggesting the presence of a parallel potential drop below the spacecraft. These electrons are collocated with upgoing ion beams with energies approaching 1–2 keV. Thus, the total inverted-V acceleration region potential drop has increased (3.1 ± 0.6 kV), a significant fraction of which is now found to extend above SC4's altitude. In the sample depicted in Figure 6d a low-energy upgoing electron beam at energies from 30 eV to 200 eV is also seen by the HEEA detector (red dashed curve in top and middle panels). This upgoing beam partially fills the loss cone, which appears less pronounced than the previous sample given in Figure 6c (e.g., compare velocity space distributions shown in Figures 6c (bottom) and 6d (bottom)). The presence of the upgoing beam is indicative of acceleration via dispersive Alfvén waves that are embedded in the inverted-V upward current system. This appears to be transient, as it is evident in only the HEEA data in Figure 6d and not in the previously sampled distribution function depicted in Figure 6c. Two other distribution examples sampled in the same large-scale upward current region a few spin periods afterward given in Figures 6e and 6f also exhibit inverted-V acceleration signatures (an enhanced energetic precipitating electron peak with modified loss cone features) superposed with Alfvén wave acceleration signatures (lower energy counterstreaming electrons). These mixed distribution characteristics suggest that Alfvén wave acceleration processes are active and are feeding into inverted-V acceleration processes near the initial onset period.

Subsequent to the initial encounter with SC4, the hot plasma expands poleward and overtakes SC2 at ~ 0038 UT and then later overtakes SC3 and SC1 near $\sim 0039:40$ UT (indicated by the magenta vertical lines in Figures 3 and 4). This poleward expansion effectively results in the gross thickening of the plasma sheet. The near-simultaneous occurrence of the injection front by SC3 and SC1 indicates that hot plasma injection front is approaching these spacecraft not just from the equatorward direction but also from the azimuthal direction. Interestingly, the upgoing hot ion plasma sheet population does exhibit a delayed occurrence relative to the downgoing injected counterpart. This is most apparent in the ion data observed by SC3 depicted in Figures 4f and 4g, where the hot upgoing plasma sheet ions show up at $\sim 0040:35$ UT, which is nearly a minute after the initial ion injection signatures are observed. We interpret this delayed response as a time-of-flight effect owing to convection and the finite time it takes for the initially downgoing ions, which are much heavier than electrons, to travel back to Cluster's altitude after they experience magnetic mirroring at lower altitudes. Transit times from Cluster to a mirror point at lower altitudes (e.g., $0.1 R_E$ – $1 R_E$ above Earth) and back for protons with pitch angles of 10° – 20° and energies ~ 5 – 10 keV are roughly estimated to be on the order of 30 s to minute time scales based on a dipole field model, which are consistent with the observed time delay.

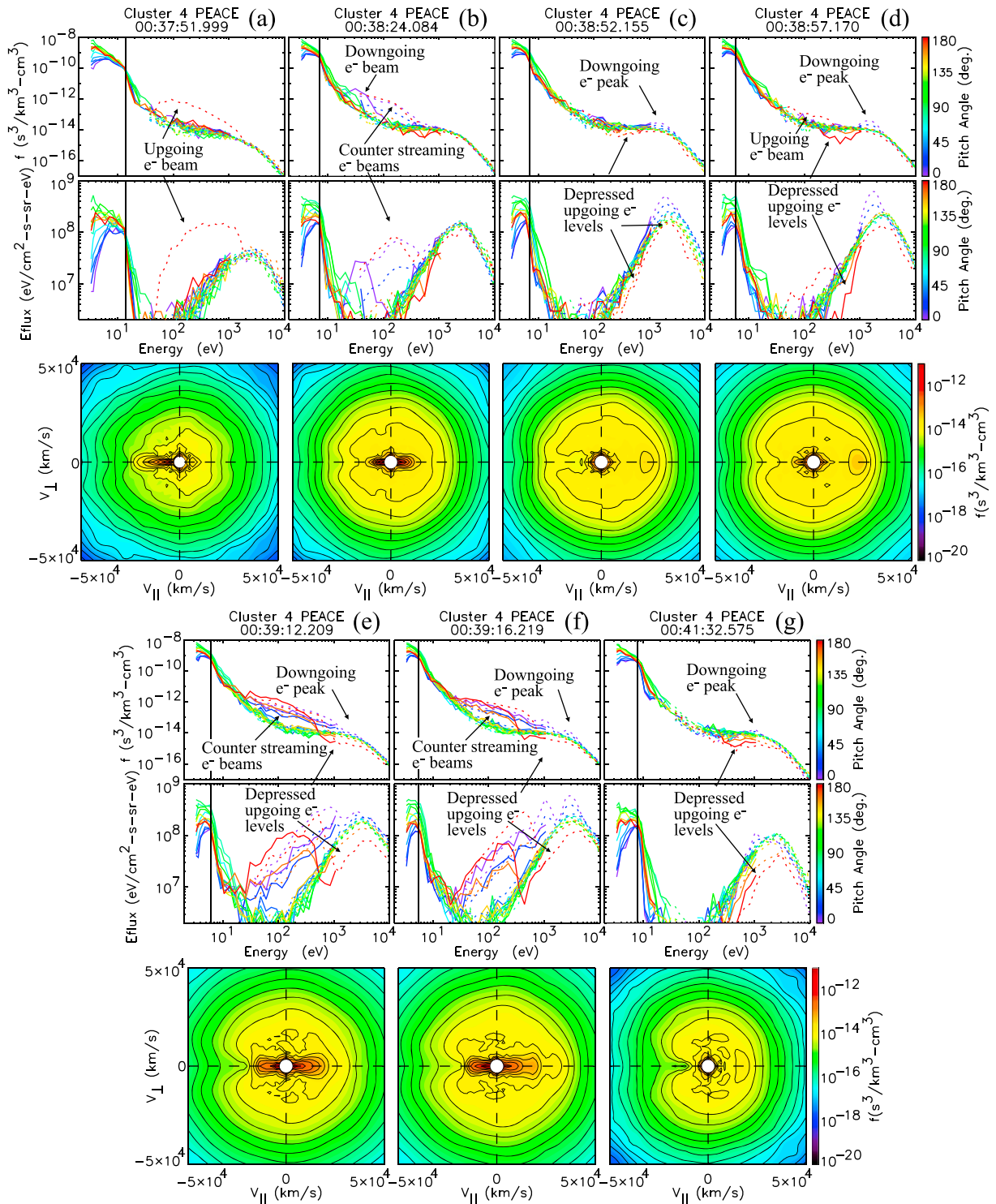


Figure 6. (a–g) (top) Electron distribution function spectra, (middle) differential energy flux spectra, and (bottom) velocity space distribution from SC4 sampled at seven different locations during its transect of the plasma sheet. The data are shown in the same format as Figure 5.

In association with the injected plasma poleward expansion, the small-scale currents within much of the Alfvén region are shown to broaden and attenuate in concert with the formation of a large-scale, inverted-V, upward current region. The developing large-scale upward current region is most apparent in the ΔB_y profiles from SC2 (red shaded interval from 0040:10 to 0043:00 UT) and SC4 (red shaded interval from 0041:10 to 0043:50 UT) shown in Figures 3k and 3o, respectively. The average background upward current density is estimated at 17 nA/m² and 24 nA/m² for SC2 and SC4, respectively. These values map to 1400 nA/m² and 2000 nA/m² at the ionosphere. The overall width of the developing large-scale upward current is estimated at 680 km and 640 km for SC2 and SC4 measurements, respectively. These map to thicknesses of 76 km and 71 km at ionospheric altitudes, which is an order of magnitude larger than the small-scale Alfvénic currents. Consistent with the formation of a stable large-scale upward current region with a potential drop below the spacecraft, the electrons display signatures of energy flux dropouts near 180° pitch angles (see Figure 3n over same interval). Moreover, no significant signatures of broad energy electron beams are observed, suggesting that acceleration via dispersive scale Alfvén waves was significantly diminished by the time SC4 traversed the region. A representative electron distribution function sampled by SC4 in this region at 0041:32.575 UT is shown in Figure 6g. Suggestive of a sizable acceleration potential above SC4, the precipitating component of the distribution function (indicated by purple in Figure 6g (top and middle)) shows a peak near 1 keV. Depressed levels in the upgoing (red curves in Figure 6g (top and middle)) electron distribution and energy flux spectra are clearly visible. These features are readily identifiable in the distribution function given in velocity space format depicted in Figure 6g (bottom). The electrons with modified loss cone features are coincident with upgoing, field-aligned ion beams (see Figure 4l over same interval). An estimate of the parallel potential drop below SC4 from the peak energy of the ion beam near the electron distribution sample is found to be ~1.7 kV. Based on these observed electron and ion characteristics together with the changes in the properties of the field-aligned currents, we conclude that the expansion process led to the formation of a large-scale inverted-V arc system, associated with a quasistatic potential drop of ~2.7 kV.

This large-scale upward current region is subsequently followed by a relatively narrow, intense downward current region (peaking at 16 nA/m²), which occurs at the poleward edge of the plasma sheet from 0043:50 to 0045 UT in Figure 3p. This relatively narrow downward current region has the characteristics of the narrow “Region 0” (R0) field-aligned current layer at the poleward boundary of the auroral bulge reported in the literature [e.g., see *Fujii et al.*, 1994; *Hoffman et al.*, 1994, and references therein]. Here we see that the R0 regions extend to the center-east part of the substorm auroral bulge a region which was not well sampled in past studies. The current intensity of this R0 current region roughly balances (~5%) the adjacent large-scale upward current system that forms. Seemingly forming before the adjacent large-scale upward current system is well developed, this downward current region is also seen by SC3 and SC2 but did not exist during SC1’s transect of the region.

3.2. Latitudinal Profiles

It is difficult to ascertain the propagation of structures as they occur and evolve based on the time profiles depicted in Figure 3. To aid in the interpretation, Figure 7 shows plasma and field data as a function of invariant latitude. These data are presented in the order each spacecraft traversed the region (SC1, SC3, SC2, and then SC4). For each spacecraft, Figure 7 shows the latitude profiles of the omnidirectional electron differential energy flux versus energy, the westward perturbation magnetic field, and the current density. As mentioned above, substorm activity was first seen on SC4 by the sudden occurrence of a fairly hot, dense plasma at an invariant latitude near $\Lambda \sim 66.7^\circ$. As made apparent in Figure 7, the injection front expanded poleward and was later observed by SC2 and then by SC3 at higher invariant latitudes (indicated by the magenta vertical lines). From interspacecraft timing analysis, the average poleward velocity of the injection boundary is roughly 10 km/s, which maps to a speed of ~1 km/s at ionospheric altitudes. This velocity is in rough accord with the poleward expansion velocity of the substorm auroral emissions, which is estimated at 0.9 ± 0.3 km/s based on latitudinal profiles. While the injection front was expanding poleward, the current systems encountered throughout the interval are moving equatorward. Two example intervals with suitably stable current systems that demonstrate this behavior are indicated by the gray shaded regions in Figures 7c, 7f, 7i, and 7l. The first interval corresponds to a large-scale, up-down current sheet pair first encountered by SC1 at an invariant latitude of 67.7° . We interpreted this current system as being associated with the PBI that occurred prior to substorm onset. Figure 7 verifies that this current system, which was first observed by SC1, was observed at later times by SC3, SC2, and then SC4 at lower invariant latitudes. From interspacecraft timings, we found that this current system was moving at an average equatorward velocity of 8 km/s in an Earth fixed frame,

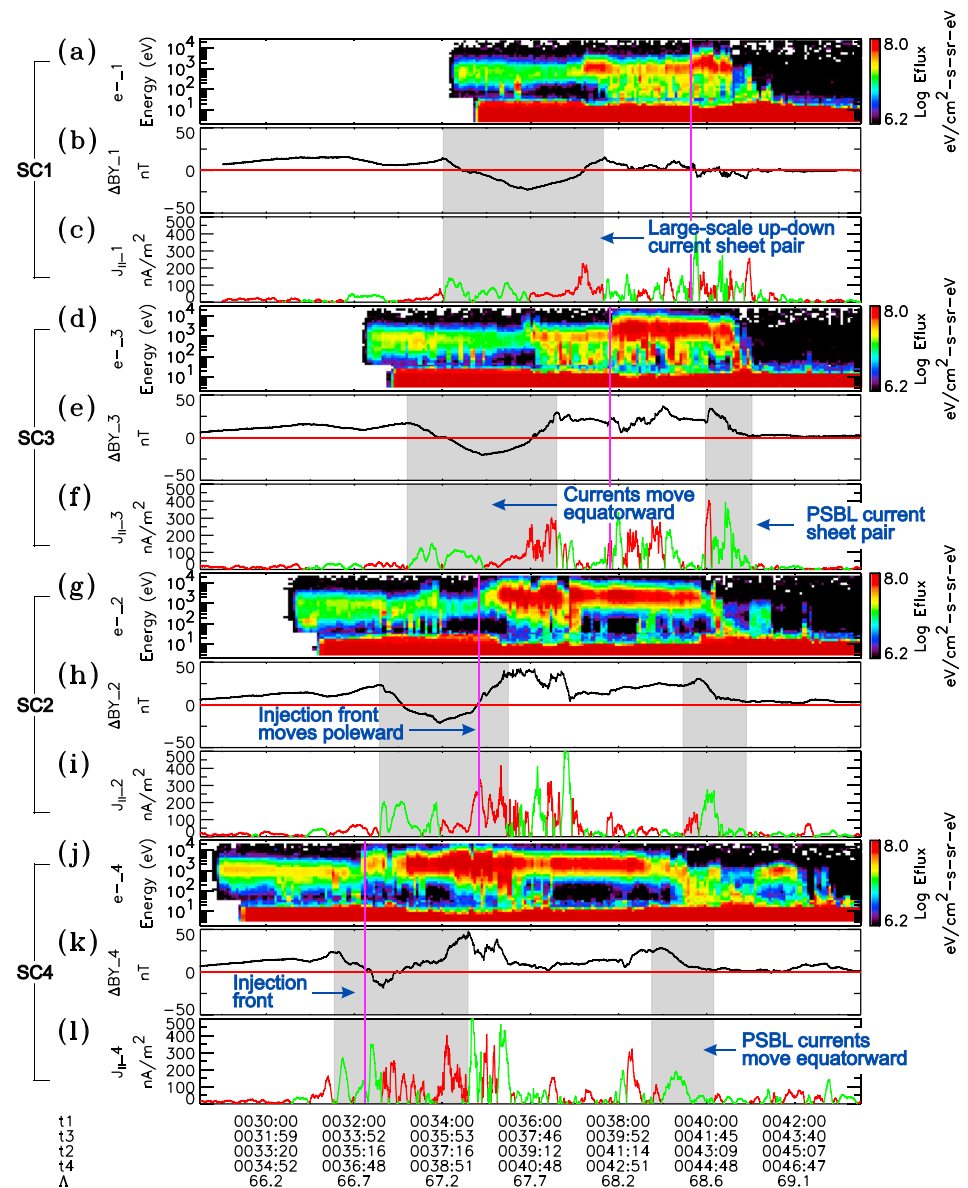


Figure 7. Invariant latitude profiles of (a, d, g, and j) the omnidirectional electron differential energy flux versus energy, (b, e, h, and k) the westward perturbation magnetic field, and (c, f, i, and l) the field-aligned current density for SC1 (Figures 7a–7c), SC3 (Figures 7d–7f), SC2 (Figures 7g–7i), and SC4 (Figures 7j–7l).

which maps down to a value of 0.9 km/s at the ionosphere. The thickness of the upward current part is estimated at ~ 90 km at the ionosphere. These results are in reasonable agreement with the equatorward velocity and thickness of the associated PBI enhancement, which are estimated to be 0.7 km/s and 130 ± 50 km, respectively, based on the latitudinal profile of emissions from MLT cuts through the Cluster foot points (not shown). A second example interval corresponds to a current sheet pair system that formed at the plasma sheet boundary layer. This current system was found to be moving equatorward at a speed of ~ 4 km/s. Unfortunately, this current system is too thin to be resolved in the auroral images.

3.3. Evolution of Electric and Magnetic Fields and Poynting Flux

Figure 8 depicts spin plane measurements of the electric fields in GSE coordinates and the parallel Poynting flux due to Alfvénic fluctuations mapped to the ionospheric altitudes from Cluster in the same time-ordered sequence used in Figure 3. Approximate substorm phase event times are indicated at the top. The injection front locations determined previously are indicated by the magenta vertical lines. Parallel current densities,

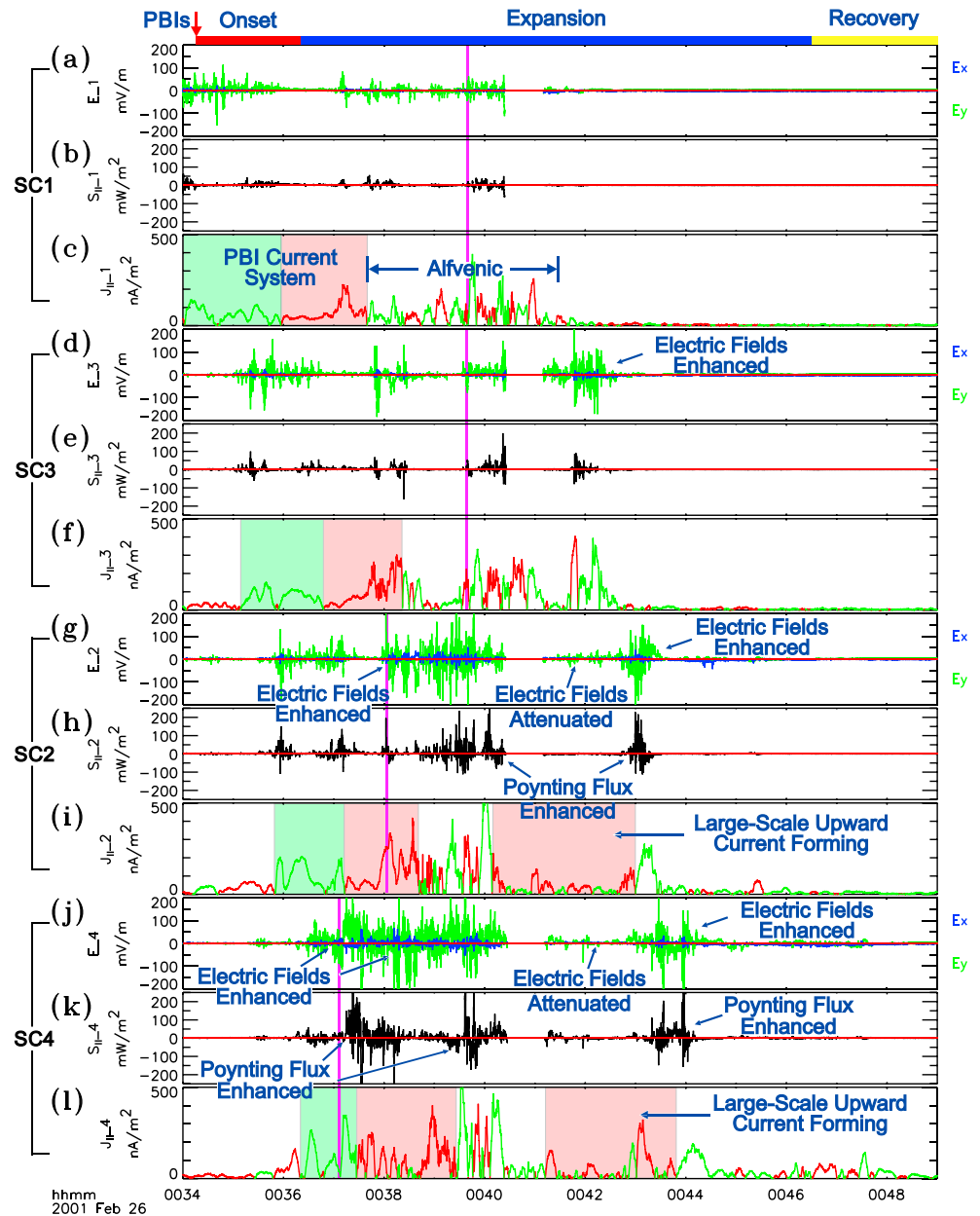


Figure 8. (a, d, g, and j) X GSE and Y GSE components of the electric fields, (b, e, h, and k) estimates of the field-aligned Poynting flux S_{\parallel} due to Alfvén waves mapped to the ionosphere (positive is earthward), and (c, f, i, and l) parallel current densities for SC1 (Figures 8a–8c), SC3 (Figures 8d–8f), SC2 (Figures 8g–8i), and SC4 (Figures 8j–8l).

including the PBI and the developing upward current shaded intervals discussed previously, are also shown as a visual reference. It is important to note that the background magnetic field is oriented nearly within the spin plane of the spacecraft along the X GSE direction (i.e., the average magnetic field unit vector sampled by SC1 in the plasma sheet is $\hat{\mathbf{b}}_1 = (0.991, 0.0895, -0.1024)$). Consequently, the north-south electric field (component in magnetic meridional plane perpendicular to the magnetic field \mathbf{B}), which is expected to be along the spin axis (Z GSE direction), is not measured nor can be reconstructed under the assumption that $\mathbf{E} \cdot \mathbf{B} = 0$ from the other measured components. Nevertheless, the X GSE and Y GSE components are well measured and correspond to the magnetic field-aligned and westward components of the electric field, respectively. Values for the parallel Poynting flux ($S_{\parallel} = (\delta \mathbf{E} \times \delta \mathbf{B}) \cdot \hat{\mathbf{b}} / \mu_0$) are estimated from the spin plane components of the electric field and all components of the perturbation magnetic field and thus is to be viewed as a lower bound estimate. The electric and magnetic field data were band-pass filtered at frequencies from 10 mHz to 11 Hz

(Nyquist limit) prior to computing S_{\parallel} . As will be demonstrated in sections 3.3.1 and 3.3.2 below, the Poynting flux in this frequency range provides a reasonable measure of contributions from Alfvénic fluctuations.

The electric fields shown in Figure 8 are quite variable, and spiky, with the dominant component being transverse to the background magnetic field (in general $E_y/E_x \gtrsim 10$). On SC1, the largest electric fields are seen in the downward current region of the PBI current system, with peak amplitudes that are generally $\lesssim 40$ mV/m, with some exceptions reaching ~ 100 mV/m (see Figure 8a). The electric fields in the Alfvén-dominated region poleward of the PBI current system have slightly smaller amplitudes, with values that are typically $\lesssim 30$ mV/m, with some exceptions reaching ~ 80 mV/m. The Alfvénic Poynting fluxes in these regions have a preferential earthward sense and have peak amplitudes at ionospheric altitudes that are generally $\lesssim 20$ mW/m², with some exceptions reaching 40–50 mW/m² (see Figure 8b). Though not perfect, enhancements in Alfvénic Poynting flux generally coincide with regions of enhanced electric field activity.

The most intense electric fields are observed by SC4 at and just after the initial injection onset location (interval from $\sim 0037:00$ – $0040:25$ UT in Figure 8j). Here the electric field amplitudes often reach 80 mV/m to 200 mV/m. A substantial increase in the Alfvénic Poynting flux levels is also observed over the same interval, with peak values ranging from 50 mW/m² to over 200 mW/m² (see Figure 8k). In contrast the electric fields (and Poynting fluxes) are seen to be attenuated (from SC1 values) over most of the region associated with the growth of the large-scale inverted-V upward current ($0041:10$ – $0042:50$ UT). This is in conjunction with the attenuation of the small-scale Alfvénic currents in the region described above in section 3.1. The electric fields and Poynting fluxes are again enhanced at the plasma sheet boundary layer region (near $0042:50$ – $0044:10$ UT), which encompasses the poleward part of the large-scale upward current region and the intense downward current region that follows, previously interpreted as part of the narrow R0 current region. Similar behavior is seen in the electric fields and Poynting fluxes from SC2 (see Figures 8g and 8h, respectively). Large electric fields and Poynting flux enhancements are observed subsequent to the hot injected plasma overtaking SC2 (from $0038:00$ to $0040:25$ UT), which are followed by attenuated values associated with the growth of the large-scale inverted-V upward current region (from $0041:10$ to $0042:50$ UT), and then enhanced values at the PSBL (from $0042:50$ – $0043:30$ UT). The electric field and Alfvénic Poynting flux values may be slightly enhanced as the injection front overtakes SC1 and SC3 near $\sim 0039:40$ UT, but this interpretation is uncertain owing to the data gap ($\sim 0040:20$ – $0041:10$). However, enhanced electric field activity is discernible in SC3 observations at the PSBL from $\sim 0041:40$ to $0042:20$ UT in Figure 8d.

3.3.1. Alfvén Wave Evolution Associated With Initial Injection

As mentioned above, the PBI current system was found to undergo dramatic changes in response to the injection process. Particularly noteworthy was the broadening and filamentation of what was initially a fairly stable current system. To understand the nature of the magnetic fluctuations associated with this evolutionary process, Figure 9a compares power spectral density (PSD) of the magnetic fields measured by SC1 in the upward current part of the PBI current system ($0036:00$ – $0037:40$ UT) to that sampled by SC4 ($0037:30$ – $0039:24$). The ratio between SC4 and SC1 magnetic field PSDs is shown in Figure 9b. The comparisons reveal that the PSD from SC4 is enhanced relative to that from SC1 over the entire frequency range, with the largest increases (by a factor of 300) occurring at frequencies >20 mHz. This frequency range encompasses the nested series of intense, small-scale currents that suddenly occur during the initial injection described above, as well as higher frequency fluctuations. The comparisons are ambiguous above ~ 230 mHz, owing to the spurious spin tone and harmonics in the spectra (dashed vertical lines) and intensities approaching FGM's sensitivity floor. The latter results in an artificial flattening of the magnetic field PSD from SC1 (and SC4) at a level of $\sim 10^{-3}$ nT²/Hz in Figure 9a. Thus, the growth in electromagnetic wave activity that occurs is not limited to a restricted frequency band but is effectively broadband. Nevertheless, the spectral trend suggests that substantial enhancements in the magnetic field fluctuations should at least persist up to 1 Hz and likely above. Note that the STAFF instrument [Cornilleau-Wehrin *et al.*, 1997], which samples higher frequency fluctuations (8 Hz–4 kHz), did not have a sample from SC1 and SC4 in the region, so we are unable to confirm the extension of the spectrum to higher frequencies. The fields associated with the macroscale inverted-V current system show moderate increases signified by a factor of 3–5 increase in the PSD ratio at frequencies <20 mHz.

To identify the fluctuations, Figure 9c depicts the ratio between orthogonal components of the electric (E_y^{FAC}) and magnetic (B_x^{FAC}) fields as a function of frequency for SC1 in the upward current part of the PBI current system and for SC4 in the same region during the initial injection onset. Note that the fields are represented in a magnetic field-aligned coordinate (FAC) system in which the x axis is in the local plane of curvature of the

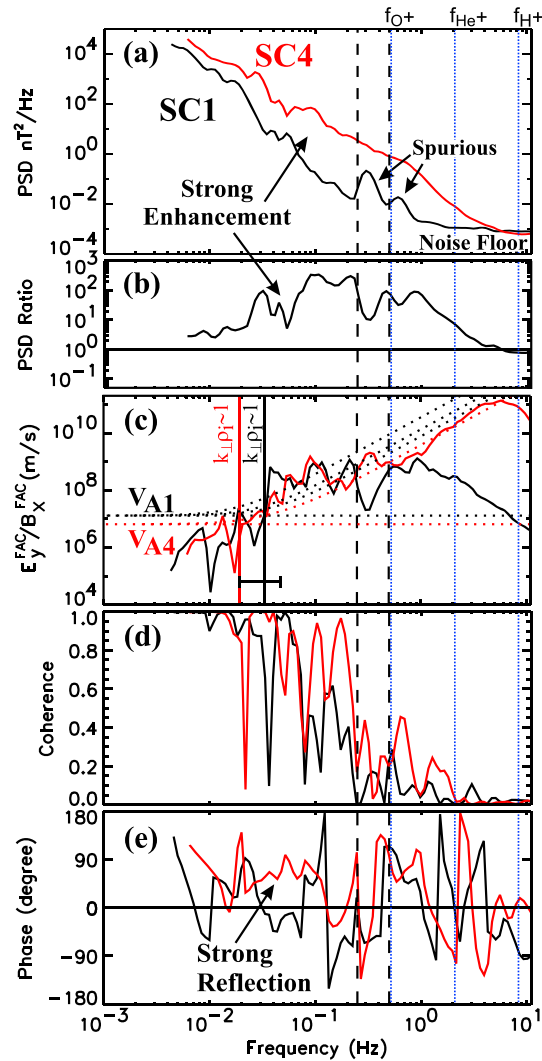


Figure 9. (a) Power spectral density (PSD) of the magnetic field as a function of frequency for SC1 (black curve) and SC4 (red curve) and (b) the ratio between the SC4 PSD and SC1 PSD. The PSDs were computed via a Morlet wavelet transform. Also shown are the (c) ratio between E_y^{FAC} and B_x^{FAC} , (d) coherence, and (e) relative phase between E_y^{FAC} and B_x^{FAC} as a function of frequency for SC1 (black curve) in the upward current part of the PBI current system and SC4 (red curve) in the region where the current striations occur. The dotted blue lines at 0.52, 2.08, and 8.32 Hz represent the H^+ , He^+ , and O^+ gyrofrequencies, respectively. The spacecraft spin frequency and harmonic are indicated by dashed vertical lines. The solid vertical lines in Figure 9c indicate where the perpendicular wavelength is on the order of the kinetic ion gyroradius scale for SC1 (black) and SC4 (red). The dotted curves in Figure 9c are the theoretical estimates of the $E_y^{\text{FAC}}/B_x^{\text{FAC}}$ ratio for SC1 (black) and SC4 (red).

background magnetic field and directed in the northward direction, the y axis is perpendicular to the magnetic meridional plane and points in the magnetic westward direction, the z axis completes the orthonormal set and is oriented antiparallel to the large-scale background magnetic field in the tailward direction. In this system the westward electric field component E_y^{FAC} is measured in the spin plane perpendicular to the background magnetic field, and the northward magnetic field component B_x^{FAC} is approximately aligned along the spin axis. As mentioned above, we used E_y^{FAC} because the north-south component of the electric field, which is nearly aligned along the spin axis for this event, is not measured. The westward component E_z^{FAC} , which is along Y GSE, is well measured enabling an assessment of the electric and magnetic field ratios, relative phases and coherency for electromagnetic waves that occur in the region.

According to SC1 data, the E - B ratio generally increases with increasing frequency before being depressed, owing to spurious spin tone and the roll-off near 1 Hz frequency, as a consequence of reaching the fluxgate

magnetometer floor. The E - B ratio from SC4 more or less overlaps that of SC1 at frequencies below the spin period ($\lesssim 0.2$ Hz). However, owing to the enhanced magnetic (and electric) field activity over the broad frequency range, the E - B ratio continues to rise almost linearly before rolling off near 6 Hz due to the FGM instrument floor. The E - B ratio at frequencies $f < 20$ mHz, which corresponds to the macroscale currents, are significantly below the Alfvén speed indicated by the horizontal dotted lines in Figure 9c. This suggests that the large-scale currents are not large-scale traveling Alfvén waves. Although part of the spectra extends up to ion cyclotron frequencies, the shape of the magnetic and electric field (not shown) PSDs taken together with the trends in the E - B ratios at higher frequencies are not consistent with the signatures of ion cyclotron waves. Such waves show up as distinct nearly monochromatic enhancements in the PSDs of the electric and/or magnetic fields at cyclotron frequencies and harmonics.

The E - B ratio at frequencies $f > 20$ mHz associated with small-scale currents are consistent with the properties of Doppler-shifted, dispersive Alfvén waves. To show this, we obtain theoretical estimates for the ratio using the following expression [Chaston *et al.*, 2003]:

$$\frac{E_{\perp 1}}{B_{\perp 2}} = V_A \sqrt{\frac{1 + k_{\perp}^2 \lambda_e^2}{1 + k_{\perp}^2 (\rho_i^2 + \rho_s^2)}} (1 + k_{\perp}^2 \rho_i^2) \quad (1)$$

Here k_{\perp} is the wave number perpendicular to the background magnetic field \mathbf{B}_0 , λ_e is the electron inertial length, ρ_i is the ion gyroradius, and $\rho_s = c_s/\omega_i$ is the ion acoustic gyroradius, where c_s is the ion acoustic speed and ω_i the ion gyrofrequency. This expression is based on the dispersion relation reported by Lysak and Lotko [1996], which was later modified by Chaston *et al.* [2003] to include finite ion gyroradius corrections. Such an approximation is in reasonable agreement with numerical-based solutions obtained from the waves in homogeneous anisotropic magnetized plasma (WHAMP) dispersion relation code. A generalized expression was used because the Cluster fleet was transiting a region, where the ratio $V_A/V_e \sim 1.5 \pm 0.5$ (according to SC1 data), which is intermediate between the inertial and kinetic Alfvén wave regime. In this region the ion gyroradius $\rho_i \sim 6$ km, the ion acoustic gyroradius $\rho_s \sim 3.8$ km, and the electron inertial length $\lambda_e \sim 6$ km are of the same order, based on local measurements of the electron and ion temperature, density, and background magnetic field from SC1. Owing to the changing boundary conditions induced by the injection process, the ion gyroradius $\rho_i \sim 14$ km, the ion acoustic gyroradius $\rho_s \sim 6.7$ km, and the electron inertial length $\lambda_e \sim 2.9$ km are more separate by the time SC4 traverses the region. Under the assumption these are primarily Doppler-shifted waves, the perpendicular wave number is related to the spacecraft frame frequency given by $f_{SC} = k_{\perp} v_r / 2\pi$, with the parameter v_r being the relative speed determinable from a fit to observed ratios. Theoretical estimates obtained using these parameters and a fit value for v_r in equation (1) are indicated by the black (SC1) and red (SC4) dotted curves that increase with frequency from V_A in Figure 9c. The observed ratio is in reasonable agreement with theoretical estimates for fluctuations at frequencies from 20 mHz to 6 Hz on SC4, which verifies that these are consistent with being Doppler-shifted, dispersive Alfvén waves. Here a value of $v_r = 1.8$ km/s was used. The solid red vertical line in Figure 9c indicates the frequency, where the perpendicular wavelength is on the order of the kinetic ion gyroradius scale. Owing to the roll-off in the ratio from SC1 near and above $f \sim 0.2$ Hz due to relatively weak magnetic field signals not well resolved by FGM, comparisons between observed and theoretical estimates at higher frequencies are inaccurate. Nevertheless, the similar behavior of the ratio from SC1 at the lower frequencies to that seen from SC4 suggests that fluctuations from 20 mHz to $f \sim 0.2$ Hz (and likely above) are also consistent with being Doppler-shifted Alfvén waves. Three theoretical estimates are given to show the possible range expected for values of v_r set to 0.75 km/s, 1.25 km/s, and 1.75 km/s, respectively. The frequency where $k_{\perp} \rho_i \sim 1$ based on $v_r = 1.25$ km/s is indicated by the black vertical line. The horizontal error bar indicates the sensitivity of this frequency based on the range of v_r used, which seems plausible given the behavior of the ratio from SC1.

Figures 9d and 9e show the coherence and the relative phase between E_y^{FAC} and B_x^{FAC} as a function of frequency for SC1 in the upward current part of the PBI current system (black curve) and SC4 in the region where the current striations occur (red curve). The coherence between E_y^{FAC} and B_x^{FAC} provides a measure of the degree to which these signals are correlated within a selected time interval. Values greater than ~ 0.7 indicate that signals are reasonably coherent, while values near zero indicate that the phase is nonstationary over the selected time interval. The relative phase spectrum shown in Figure 9e indicates the degree to which fluctuations within a given frequency can be described as being purely propagating or shows signs of reflection. Values for the relative phase near 0° , $\pm 180^\circ$ indicate a freely propagating wave. Significant departures from

these values indicate interference between incoming and reflected waves from the ionosphere and/or steep gradients along the magnetic field. In the limit where the value of the relative phase is near $\pm 90^\circ$ the interference results in a standing wave pattern. Clearly, the coherence and phase spectra are sensitive to the time interval used in the computation. We chose a window that is optimal for the characterization of the short-scale Alfvénic fluctuations. The relative phase is inaccurate and should not be trusted when values of the coherency and/or PSDs are low, such as in the interval from 0.2 Hz to 11 Hz in Figure 9. The comparisons show that the electric and magnetic field fluctuations observed on SC4 are associated with strong interference (standing wave) signatures with relative phases approaching 90° over a broader range of frequencies. This is particularly noticeable in the frequency range from ~ 30 –100 mHz, which is associated with the intense dispersive Alfvén waves that led to the striations in current observed in the SC4 data. In contrast, the dispersive Alfvén wave fluctuations seen by SC1 in the same 30–100 mHz frequency range show some evidence of traveling wave behavior, with the relative phase approaching near zero collocated with the coherence peak near 1 in the interval. Moreover, local maxima in the E - B ratio from SC4 are generally collocated with relative phases that depart significantly from 0° . This suggests that the enhancements/peaks in the ratio may be an effect attributed to the interference of incoming and outgoing waves.

3.3.2. Alfvén Wave Evolution Associated With Inverted-V Current Formation

The poleward expansion of injected plasma is associated with the development of a large-scale inverted-V arc system of field-aligned currents out of a region initially dominated by Alfvénic fluctuations. The Alfvénic currents were noticeably attenuated during this process. The frequency regimes associated with the growth and attenuation of currents is made apparent in Figures 10a and 10b. Comparisons between the PSD of magnetic fields measured by SC1 in the Alfvén-dominated region (0038:20–0041:00 UT) and that sampled by SC4 in the plasma sheet where the new large-scale, inverted-V arc current system forms (0041:00–0044:00 UT) are shown in Figure 10a. The ratio between SC4 and SC1 magnetic field PSDs is shown in Figure 10b. Interestingly, the magnetic field fluctuations observed by SC1 in the Alfvén-dominated region have a PSD spectrum (black curve in Figure 10a) at frequencies > 20 –30 mHz that is very similar in amplitude and slope to the magnetic field PSD spectrum observed by SC4 during the initial injection (red curve in Figure 9a). This frequency regime encompasses the nested series of intense, small-scale Alfvénic currents (20 mHz–100 mHz) in the Alfvén region, which occurs poleward of and is eventually overtaken by the newly injected energetic plasma by the time SC4 crosses the region. The comparisons in Figures 10a and 10b reveal that the PSD from SC4 is moderately enhanced (up to factor 3.5) relative to that from SC1 at frequencies < 20 mHz, in association with the growth of the large-scale, field-aligned current system in the region. This growth is accompanied by up to an order of magnitude attenuation of fluctuations at frequencies > 20 mHz. While the intensities have attenuated, the PSD spectrum is still elevated at frequencies > 20 mHz compared to that observed by SC1 in the upward current part of the PBI arc system depicted in Figure 9a. Thus, remnants of the induced field-aligned currents associated with these fluctuations are still found to be embedded in the growing large-scale current system, even though as mentioned above their influence in accelerating electrons has been significantly diminished. Note that the comparisons are ambiguous at frequencies above ~ 4 Hz, owing to the intensities approaching FGM's sensitivity floor (near $\sim 10^{-3}$ nT²/Hz). The STAFF instrument did not have a sample in the Alfvén region crossed by SC1. However, power spectral densities from STAFF during SC4's traversal of the forming upward current region are available and show that the magnetic field fluctuations extend up to 20–30 Hz (not shown).

Figure 10c shows the ratio between perpendicular components of the electric field E_y^{FAC} and the magnetic field B_x^{FAC} as a function of frequency for SC1 in the Alfvén-dominated region and for SC4 in the developing inverted-V region. According to SC1 data, the E - B ratio at frequencies $f < 20$ mHz show strong enhancements that significantly depart from the Alfvén speed V_A . This frequency corresponds to the relatively large-scale inverted-V arc current systems. At frequencies between $25 \text{ mHz} \leq f \leq 100 \text{ mHz}$, the E - B ratio appears to be nearing a plateau just below the Alfvén speed and then rises sharply before reaching a roll-off near 2–3 Hz. The roll-off is largely attributed to the magnetic field reaching the noise level. A sharp rise in the E - B ratio from V_A with increasing frequency for fields measured by SC4 is also seen. However, in this case the rise occurs at a lower frequency (near $f = 30$ mHz). The sharp increase in the ratios with increasing frequency from both spacecraft suggests that the waves at these frequencies are Doppler-shifted, dispersive Alfvén waves. This identification is supported by the reasonable agreement between the observed values and theoretical estimates based on equation (1), including the shift of the ratio from SC4 to lower frequencies. A reasonable fit is

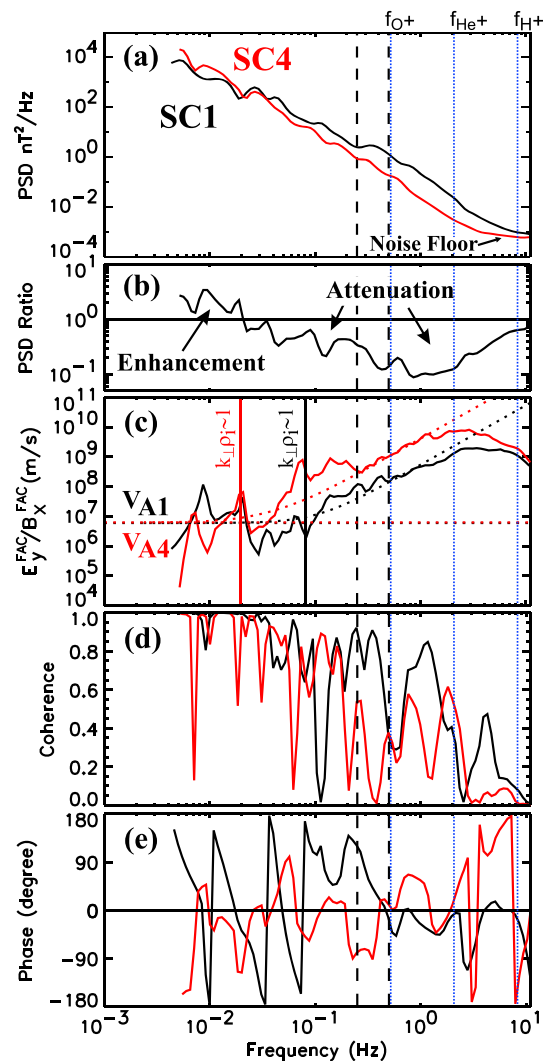


Figure 10. Magnetic field PSDs, the PSD ratio, the E_y^{FAC} to B_x^{FAC} ratio, coherence and relative phase for SC1 in the Alfvén-dominated region (black curve) and SC4 in the plasma sheet where the new large-scale, inverted-V arc current system forms (red curve) in same format as Figure 9.

obtained from equation (1) using local values for density, temperature, and magnetic fields and with relative speeds of $v_{r1} \sim 3.0$ km/s and $v_{r4} \sim 1.4$ km/s for SC1 and SC4, respectively. These comparisons suggest that the attenuation of the Alfvénic currents during the growth of the large-scale current system is due to Alfvén waves becoming dispersive at larger perpendicular scales and thus susceptible to damping by virtue of the changing plasma conditions induced by the injection process. Another contributing factor may be that its distant driving mechanism/source may not be constant but may be transient, being active only during the initial stages of substorm development.

To investigate the propagation characteristics of the waves, Figures 10d and 10e show the coherence and the relative phase between E_y^{FAC} and B_x^{FAC} as a function of frequency for SC1 (black curve) in the Alfvén region and SC4 in the same region during the formation of the large-scale upward current region (red curve). Although there are peaks in the coherence that are near one, it is important to note that the phase spectrum is inaccurate at frequencies near the spin tone and at frequencies $\gtrsim 1-2$ Hz, where the fluctuations are approaching FGM's instrument floor. The phase spectrum from SC1 shows strong variations, which appear to be the result of admixtures of downgoing (phases near 0°), upgoing (phases near $\pm 180^\circ$), and standing Alfvén wave patterns. The phase spectrum from SC4 is also quite variable; however, the variations alternate between standing wave (phases near $\pm 90^\circ$) and incoming wave (phases near 0°) characteristics.

4. Discussion

The multipoint observations reveal that substorm current system formation and evolution is a dynamic multi-scale, injection-mediated process, whereby a relatively cool tenuous plasma gets replaced by a denser, hotter, and more energetic magnetospheric population. It is a process in which both inverted-V and Alfvénic acceleration mechanisms play active roles. These acceleration processes are not necessarily mutually exclusive but are found to be dynamically linked. This close connection is first indicated near the initial onset period, which is characterized by the gross intensification and filamentation of a preexisting quasistatic arc current system to smaller-scale/dispersive Alfvén waves in response to the sudden injection of a denser, hotter, and more energetic magnetospheric population. The sequence of events is consistent with the notion that the small-scale/dispersive Alfvén waves may be generated from larger-scale Alfvén waves and/or the destabilization of the macroscale current. In addition to imparting substructure on larger-scale field-aligned currents, the Alfvén waves that reach dispersive scales can accelerate the plasma locally and thus provides a means for energy transfer from larger-scale structure into the plasma in this paradigm. Such an evolutionary sequence is suggested in theoretical models [e.g., for a discussion of candidate models see *Chaston et al.*, 2011, and references therein] or single spacecraft data [e.g., *Wygant et al.*, 2002], but evidence of such a process has not been seen in multispacecraft data until now. Depending on location, prominent Alfvén acceleration, quasistatic acceleration, or a mixture of both are found to be active in this fragmented PBI current system. The latter case is similar in nature to mixed wave and quasistatic acceleration signatures seen in electron distributions within the acceleration region at much lower altitudes (i.e., ~ 4000 km from FAST [e.g., *McFadden et al.*, 1999; *Paschmann et al.*, 2003]). Our observations indicate that such mixed signatures can be seen at much higher altitudes. Moreover, the collocation with enhanced dispersive Alfvén wave activity indicates that Alfvén acceleration processes are active simultaneously and feeding into inverted-V acceleration processes during the initial onset/early expansion phase of the substorm. These acceleration processes in turn are shown to result in strong local enhancements in substorm auroral emissions.

Another manifestation of the close connection between Alfvénic and inverted-V processes is indicated during the poleward/eastward expansion of substorm auroral emissions, which is found to be associated with the formation of a new large-scale inverted-V FAC current system out of an initial Alfvén wave-dominated region of field-aligned currents. Alfvén-dominated regions at the poleward boundary of the substorm auroral bulge have been reported [e.g., *Wygant et al.*, 2000; *Keiling et al.*, 2005; *Haerendel and Frey*, 2014]. The multipoint observations shown here reveal that such regions may be an important transitional stage of development of large-scale, inverted-V field-aligned currents that compose the substorm current wedge system.

The initial occurrence and subsequent attenuation of the Alfvénic currents associated with the growth of the large-scale current is similar to the sequence of events reported by *Hull et al.* [2010]. In that study the growth of a new large-scale up-down current system at the PSBL, associated with a PBI during quiet time, was accompanied by the attenuation of small-scale Alfvén fluctuations. The attenuation was interpreted to be a damping effect attributed to the perpendicular scale size of the Alfvénic fluctuations becoming smaller than the electron inertial length scale, which increased as a density cavity formed. The growth of the quasistatic current system, and associated quasistatic potentials was an injection-mediated process, which led to the local expansion of the plasma sheet. Here multiple spacecraft observations indicate that the Alfvénic fluctuations became dispersive at lower frequencies (larger perpendicular scales) owing to the changing conditions induced by the sudden occurrence of a denser, hotter energetic plasma injection. The results reported here extends the initial findings by *Hull et al.* [2010] to active substorm times. These combined results suggest that Alfvénic activity may be an important precursor and perhaps may be playing an essential role in accelerating/preheating of the plasma and the development of larger-scale inverted-V arc systems during both quiet and active times.

A consequence of the injection near onset on field lines tied to the preexisting PBI current system was a sizable increase in the total upward current region potential drop, with a significant fraction being above Cluster's altitude of $3.4R_E$. This is in contrast to earlier crossings, which showed that the potential was smaller and predominantly below the Cluster spacecraft. The extension to high altitudes is above the statistical limit determined by *Mozer and Hull* [2001], who showed that the upward current acceleration region was nominally at much lower altitudes. *Li et al.* [2014] also indicated electric fields associated with quasistatic acceleration tend to occur at altitudes below $2.8 R_E$, while intense electric fields associated with Alfvénic acceleration processes tend to predominate at altitudes above $3.0 R_E$. Nevertheless, evidence of important contributions to the total acceleration potential attributed to quasistatic acceleration processes at and above Cluster's altitude

have been reported in the recent statistical study by *Alm et al.* [2015]. The growth and extension of confined auroral acceleration regions inferred from the remote observations of auroral kilometric radiation (AKR) during substorm onset have been reported in previous studies [e.g., *Morioka et al.*, 2009, 2010]. These studies showed that the vertical evolution of the auroral acceleration region from AKR is due to a two-step process: (1) a gross expansion of the preexisting auroral acceleration region at low altitude and (2) the abrupt development of a new acceleration region above this preexisting region. The latter was considered to be an identifying feature of substorm aurora. The altitude ranges over which these signatures are manifested are from 0.6 to $0.8 R_E$ and 1 to $2 R_E$, respectively, which is well below the altitude of the event reported in this paper. We cannot determine the potential distribution along the magnetic field from the measurements reported here. Thus, we do not know whether there are layers of concentrated acceleration potentials developing below, at, or above Cluster. However, we can say that vertical evolution is occurring in a manner very similar to that reported in these AKR-based studies. Here we show that the change in the altitude distribution is associated with the injection of new hot magnetospheric plasma, and the intensification and filamentation of a preexisting current system, resulting in the growth of intense Alfvénic activity in the region. The effect of these and other processes in the vertical evolution of the inverted-V acceleration potential is not fully understood and requires further study.

During an azimuthal transect by Cluster, *Forsyth et al.* [2014] demonstrated that the large-scale upward and downward field-aligned currents associated with the substorm current wedge are superposed with quasi-stationary, small spatial scale current sheets that were predominantly north-south aligned. This substructure was interpreted as drifting quasistatic current sheets in the upward current region, owing to the lack of broadband acceleration signatures in electron measurements. However, it was conjectured that the substructure in the net downward current region may be composed of quasistatic and Alfvénic signatures. The nested series of intense, small-scale currents reported here have similar spatial scales to those reported in the paper by *Forsyth et al.* [2014]. However, in our case the nested series of small-scale currents are due to interfering incoming and reflecting Alfvén waves, including during the development of the large-scale upward current region, where the amplitudes have been attenuated to the point where they are no longer effective in accelerating the plasma. We found that the small-scale current sheets had orientations that varied considerably with latitude from spacecraft to spacecraft. For example, on SC1 the currents were predominantly east-west aligned near the polar cap boundary and transitioning to north-south alignment and then back to east-west alignment with further penetration into the plasma sheet toward the PBI current system. These orientations changed during the evolutionary process. Interestingly, the nested currents found in the Alfvén-dominated region have characteristics that are similar to those found in association with the local expansion of the plasma sheet boundary layer during the recovery phase of a substorm documented by *Aikio et al.* [2008]. The spectral nature of the currents in that paper were not addressed. Nevertheless, the electrons did exhibit Alfvénic acceleration signatures. This suggests that the Alfvénic activity may be an important feature of the early makeup of expansions in the plasma sheet.

5. Summary and Conclusions

This study utilized the unique multipoint capabilities of Cluster in combination with global auroral images from IMAGE to study the spatial structure and dynamical evolution of current systems, associated acceleration processes, and constituent reorganization of the plasma that transpire within the high-altitude auroral region of the center-east part of a developing substorm auroral bulge. Key results documented in this paper are as follows:

1. Substorm onset was preceded by the occurrence of multiple poleward boundary intensifications (PBIs) and the subsequent development/progression of a streamer toward the growth phase arc. This sequence indicates that this event is of the PBI-triggered class of substorms documented in the literature.
2. The up-down current pair of one of the PBIs was sampled by the Cluster fleet (the upward current part occurred poleward of the downward current part). This current pair was shown to be composed of sheets of current that are preferentially east-west aligned and propagating equatorward at an average velocity of 8 km/s. The velocity and thicknesses, when mapped to the ionosphere, are consistent with estimates based on latitudinal profiles of emissions sampled by IMAGE, which strongly suggests that the currents and PBI are causally connected. The current pair system was found to be balanced with little (0.4%) net current, suggesting that the system is meridionally closed. The plasma was found to be cold and tenuous. The downward current region potential drop below the spacecraft estimated from upgoing electron beams was found to

be ~ 100 – 200 eV. During the initial encounter by SC1, the total potential drop in the upward current part, estimated to be ~ 1.3 keV, was found to be primarily below the spacecraft. The upward current part of the current sheet pair was also found to be embedded with small amplitude dispersive Alfvén wave fluctuations at frequencies $\gtrsim 20$ MHz. Based on the relative phase between the electric and magnetic fields, these waves were shown to exhibit incoming traveling wave signatures. No apparent signatures of Alfvén accelerated electron beams were observed, suggesting that their amplitudes were not sufficient to effectively accelerate the plasma.

3. The initial onset/early expansion period is signified by the injection of a new hot, dense, and more energetic population of magnetospheric plasma in the region tied to the preexisting PBI current system. The PBI current system, acceleration potentials, and plasma were found to undergo dramatic changes in response to the injection process. Namely, this process resulted in the broadening, intensification, and breakup of the PBI upward current into two parts: (1) A region at the leading edge of the injection, where the upward current system filamented/striated to smaller-scale/dispersive Alfvén waves, and (2) a region intensified upward current, characterized by sizable inverted-V acceleration potential drop (3.1 keV), with a significant fraction extending above the spacecraft. In the former region the electron distributions showed prominent Alfvén acceleration signatures that varied in concert with current variations, whereas in the latter region inverted-V acceleration signatures, or at times a mixture of both types of acceleration signatures were observed. Cases where mixed signatures are observed indicate that Alfvén acceleration processes contribute to and/or feed inverted-V acceleration processes during the initial onset. In contrast to the results found during SC1's transect of the region, the PBI current pair system, which is characterized by a 50% net positive upward integrated current, is no longer balanced during the injection onset occurring on SC4. This may indicate that in addition to being closed locally via meridional currents to the adjacent downward current region, the upward current part may be partially nonlocally connected via westward currents in the ionosphere to downward currents elsewhere (e.g., eastward) in the oval [Marklund *et al.*, 1998, 2012]. However, another likely explanation is that one of the currents substantially changed during the total time the spacecraft took to cross the current pair system. The growth of the Alfvén wave fluctuations was significant (with up to a factor of 300 increase in the magnetic field PSD at frequencies $20 \text{ MHz} \lesssim f \lesssim \text{few hertz}$), whereas moderate growth of the background current system (factor of 3–5) was observed. The Alfvén waves have transverse scales ranging from a few tens of kilometers to below the ion gyroradius and are associated with large electric fields (up to 200 mV/m) and large Poynting fluxes (up to 200 mW/m² mapped at ionospheric altitudes), preferentially toward Earth. The fluctuations in the frequency range from ~ 30 to 100 MHz responsible for the strong striations in the background current are associated with strong interference (standing wave) signatures with relative phases approaching 90° over a broader range of frequencies, which may be indicative of the development of a field line resonance. These observed features coincided with the strong localized brightening of emissions in the vicinity of the Cluster foot points. The observed sequence indicates that the initial PBI activations and subsequent evolution are an intrinsic part of the global auroral substorm response to injection and accompanying wave energy input from the magnetotail.
4. Poleward of the PBI current system, a broad region dominated by Alfvén wave acceleration is observed, as evidenced by the occurrence of short spatial scale variable currents together with energy dispersed, counterstreaming electrons, and low-energy ion outflow. This region, which was initially observed by the lead spacecraft SC1 during the substorm expansion phase, preceded any signs of injection. The occurrence of this region poleward of the PBI system indicates that new Alfvénic current systems are forming and propagating equatorward in the wake of the PBI current system. The Alfvén fluctuations, which occur at frequencies $\gtrsim 20$ MHz, were shown to be dispersive at frequencies $\gtrsim 100$ MHz, as evidenced by the nonlinear rise of the E - B ratio. The phase spectrum showed strong variations, which appear to be the result of admixtures of downgoing (phases near 0°), upgoing (phases near $\pm 180^\circ$), and standing Alfvén wave patterns. It is unclear whether these are forming field line resonances, as this region appears to be at the poleward edge of an expanding plasma sheet based on the location of the lead spacecraft foot point in the auroral images. The fact that the magnetic field PSD associated with the Alfvénic fluctuations has a similar spectral shape to that associated with the Alfvén waves observed at the leading edge of the initial onset injection suggest that the fluctuations in the Alfvén region may be from the same distant magnetotail source.
5. Poleward expansion of substorm emissions coincided with the poleward expansion of the hot injected plasma with poleward expansion velocities in an Earth fixed frame found to be ~ 1 km/s at ionospheric altitudes. This process resulted in the gross expansion of the plasma sheet and development of a new

large-scale inverted-V upward current region out of the Alfvén-dominated region. The growth of the large-scale current system (viewed as part of the upward current leg of the substorm current wedge) coincided with the attenuation (up to a factor of 10 decrease in magnetic field PSD) of the Alfvén fluctuations. During this transition, the electrons were shown to have less variability as they evolved to a modified loss cone distribution. We presented evidence that suggests that the attenuation of the Alfvén currents is due to Alfvén waves becoming dispersive at lower frequencies (larger perpendicular scales) and thus were susceptible to damping by virtue of the changing plasma conditions induced by the injection process. Another contributing factor may be that its distant driving source is not constant but may be transient, being active only during the initial stages of substorm development. The *E-B* phase spectrum is also quite variable; however, the variations alternate between standing wave (phases near $\pm 90^\circ$) and incoming wave (phases near 0°) characteristics.

6. A downward current region (denoted as R0) was observed to form at the poleward edge of the plasma sheet. This current system forms before the adjacent large-scale upward current system is well developed. Here we see that the R0 regions extends to the center-east part of the substorm auroral bulge a region, which was not well sampled in past studies [e.g., see Fujii *et al.*, 1994; Hoffman *et al.*, 1994, and references therein]. Ultimately, the current intensity of this R0 current region roughly balances ($\sim 5\%$) the adjacent large-scale upward current system that forms. The PSBL region, which is in part composed by this R0 current region, is associated with large electric fields and large Alfvénic Poynting flux levels similar to results of past observations [Wygant *et al.*, 2000; Keiling *et al.*, 2003].
7. Although the hot plasma expands poleward, the current systems are shown to be propagating equatorward. So it is not the poleward movement of an existing inverted-V current system that is responsible for the poleward expansion of emissions, but the development of a new large-scale arc system. A parallel potential develops via the need for hot magnetospheric electrons to maintain current continuity in an increasing magnetic field. This large-scale arc system is embedded with short spatial scale Alfvénic currents which continue to change and deform as they propagate equatorward. It is expected that these small-scale currents will lead to fine-scale substructure in the large-scale discrete arc auroral emissions with similar propagation characteristics. Unfortunately, such behavior is not resolved by the IMAGE data.

These unique multipoint observations give us a glimpse of the dynamical behavior of the auroral acceleration region during the onset and expansion phase of a substorm never before realized by single spacecraft data. To establish whether the temporal sequence documented here is characteristic of substorms or just a special case will require more multipoint case studies.

Acknowledgments

Funding for this work was provided by NASA grant NNX07AG41G and NSF grant S013865-U. We thank Cluster instrument teams and the Cluster Science Archive for providing Cluster data (<http://www.cosmos.esa.int/web/csa/>). IMAGE FUV data used in this paper are publicly available at the UC Berkeley Space Science Laboratory website (<http://sprg.ssl.berkeley.edu/image/>). Wavelet software was provided by C. Torrence and G. Compo and is available at <http://paos.colorado.edu/research/wavelets/>.

References

- Aikio, A. T., *et al.* (2004), Temporal evolution of two auroral arcs as measured by the Cluster satellite and coordinated ground-based instruments, *Ann. Geophys.*, **22**, 4089–4101.
- Aikio, A. T., T. Pitkänen, D. Fontaine, I. Dandouras, O. Amm, A. Kozlov, A. Vaivads, and A. Fazakerley (2008), EISCAT and Cluster observations in the vicinity of the dynamical polar cap boundary, *Ann. Geophys.*, **26**, 87–105.
- Akasofu, S. I. (1964), The development of the auroral substorm, *Planet. Space Sci.*, **12**, 273–282.
- Alm, L., B. Li, G. T. Marklund, and T. Karlsson (2015), Statistical altitude distribution of the auroral density cavity, *J. Geophys. Res. Space Physics*, **120**, 996–1006, doi:10.1002/2014JA020691.
- Angelopoulos, V., *et al.* (2008), Tail reconnection triggering substorm onset, *Science*, **321**, 931–935, doi:10.1126/science.1160495.
- Angelopoulos, V., *et al.* (2009), Response to comment on “tail reconnection triggering substorm onset, *Science*, **324**, 1391, doi:10.1126/science.1168045.
- Baker, D. N., T. I. Pulkkinen, V. Angelopoulos, W. Baumjohann, and R. L. McPherron (1996), Neutral line model of substorms: Past results and present view, *J. Geophys. Res.*, **101**, 12,975–13,010.
- Balogh, A., *et al.* (1997), The Cluster magnetic field investigation, *Space Sci. Rev.*, **79**, 65–91.
- Chaston, C. C., J. W. Bonnell, C. W. Carlson, J. P. McFadden, R. J. Strangeway, and R. E. Ergun (2003), Kinetic effects in the acceleration of auroral electrons in small scale Alfvén waves: A FAST case study, *Geophys. Res. Lett.*, **30**, 1289, doi:10.1029/2002GL015777.
- Chaston, C. C., K. Seki, T. Sakanoi, K. Asamura, M. Hirahara, and C. W. Carlson (2011), Cross-scale coupling in the auroral acceleration region, *Geophys. Res. Lett.*, **38**, L20101, doi:10.1029/2011GL049185.
- Cornilleau-Wehrin, N., *et al.* (1997), The Cluster Spatio-Temporal Analysis of Field Fluctuations (STAFF) experiment, *Space Sci. Rev.*, **79**, 107–136, doi:10.1023/A:1004979209565.
- Elphinstone, R. D., *et al.* (1995), Observations in the vicinity of substorm onset: Implications for the substorm process, *J. Geophys. Res.*, **100**, 7937–7969, doi:10.1029/94JA02938.
- Erickson, G. M., N. C. Maynard, W. J. Burke, G. R. Wilson, and M. A. Heinemann (2000), Electromagnetics of substorm onsets in the near-geosynchronous plasma sheet, *J. Geophys. Res.*, **105**(A11), 25,265–25,290.
- Forsyth, C., and A. N. Fazakerley (2012), Multispacecraft observations of auroral acceleration by Cluster, in *Auroral Phenomenology and Magnetospheric Processes*, *Geophys. Monogr. Ser.*, vol. 197, edited by A. Keiling *et al.*, pp. 261–270, AGU, Washington, D. C., doi:10.1029/2011GM001166.
- Forsyth, C., *et al.* (2014), In situ spatiotemporal measurements of the detailed azimuthal substructure of the substorm current wedge, *J. Geophys. Res. Space Physics*, **119**, 927–946, doi:10.1002/2013JA019302.

- Fujii, R., R. A. Hoffman, P. C. Anderson, J. D. Craven, M. Sugiura, L. A. Frank, and N. C. Maynard (1994), Electrodynamic parameters in the nighttime sector during auroral substorms, *J. Geophys. Res.*, **99**, 6093–6112, doi:10.1029/93JA02210.
- Gustafsson, G., et al. (1997), The electric field and wave experiment for the Cluster mission, *Space Sci. Rev.*, **79**, 137–156.
- Haerendel, G., and H. U. Frey (2014), Role and origin of the poleward Alfvénic arc, *J. Geophys. Res. Space Physics*, **119**, 2945–2962, doi:10.1002/2014JA019786.
- Henderson, M. G. (2009), Observational evidence for an inside-out substorm onset scenario, *Ann. Geophys.*, **27**, 2129–2140, doi:10.5194/angeo-27-2129-2009.
- Henderson, M. G. (2012), Auroral substorms, poleward boundary activations, auroral streamers, omega bands, and onset precursor activity, in *Auroral Phenomenology and Magnetospheric Processes*, *Geophys. Monogr. Ser.*, vol. 197, edited by A. Keiling et al., pp. 39–54, AGU, Washington, D. C., doi:10.1029/2011GM001165.
- Hoffman, R. A., R. Fujii, and M. Sugiura (1994), Characteristics of the field-aligned current system in the nighttime sector during auroral substorms, *J. Geophys. Res.*, **99**, 21,303–21,325, doi:10.1029/94JA01659.
- Hull, A. J., M. Wilber, C. C. Chaston, J. W. Bonnell, J. P. McFadden, F. S. Mozer, M. Fillingim, and M. L. Goldstein (2010), Time development of field-aligned currents, potential drops and plasma associated with an auroral poleward boundary intensification, *J. Geophys. Res.*, **115**, A06211, doi:10.1029/2009JA014651.
- Hwang, K.-J., M. L. Goldstein, T. E. Moore, B. M. Walsh, D. G. Baishev, A. V. Moiseyev, B. M. Shevtsov, and K. Yumoto (2014), A tailward moving current sheet normal magnetic field front followed by an earthward moving dipolarization front, *J. Geophys. Res. Space Physics*, **119**, 5316–5327, doi:10.1002/2013JA019657.
- Johnstone, A. D., et al. (1997), PEACE: A plasma electron and current experiment, *Space Sci. Rev.*, **79**, 351–398.
- Kalmoni, N. M. E., I. J. Rae, C. E. J. Watt, K. R. Murphy, C. Forsyth, and C. J. Owen (2015), Statistical characterization of the growth and spatial scales of the substorm onset arc, *J. Geophys. Res. Space Physics*, **120**, 8503–8516, doi:10.1002/2015JA021470.
- Keiling, A., J. R. Wygant, C. A. Cattell, F. S. Mozer, and C. T. Russell (2003), The global morphology of wave Poynting flux: Powering the aurora, *Science*, **299**, 383–386.
- Keiling, A., G. K. Parks, J. R. Wygant, J. Dombeck, F. S. Mozer, C. T. Russell, A. V. Streltsov, and W. Lotko (2005), Some properties of Alfvén waves: Observations in the tail lobes and the plasma sheet boundary layer, *J. Geophys. Res.*, **110**, A10S11, doi:10.1029/2004JA010907.
- Keiling, A., et al. (2002), Correlation of Alfvén Poynting flux in the plasma sheet at 4–7 R_E with ionospheric electron energy flux, *J. Geophys. Res.*, **107**(A7), 1132, doi:10.1029/2001JA000140.
- Kepko, L., E. Spanswick, V. Angelopoulos, E. Donovan, J. McFadden, K.-H. Glassmeier, J. Raeder, and H. J. Singer (2009), Equatorward moving auroral signatures of a flow burst observed prior to auroral onset, *Geophys. Res. Lett.*, **36**, L24104, doi:10.1029/2009GL041476.
- Kistler, L. M., et al. (2002), Motion of auroral ion outflow structures observed with Cluster and IMAGE FUV, *J. Geophys. Res.*, **107**(A8), 1186, doi:10.1029/2001JA005075.
- Kletzing, C. A., and J. D. Scudder (1999), Auroral-plasma sheet electron anisotropy, *Geophys. Res. Lett.*, **27**(7), 971–974.
- Li, B., G. Marklund, L. Alm, T. Karlsson, P.-A. Lindqvist, and A. Masson (2014), Statistical altitude distribution of Cluster auroral electric fields, indicating mainly quasi-static acceleration below 2.8 R_E and Alfvénic above, *J. Geophys. Res. Space Physics*, **119**, 8984–8991, doi:10.1002/2014JA020225.
- Liang, J., E. F. Donovan, W. W. Liu, B. Jackel, M. Syrjäso, S. B. Mende, H. U. Frey, V. Angelopoulos, and M. Connors (2008), Intensification of preexisting auroral arc at substorm expansion phase onset: Wave-like disruption during the first tens of seconds, *Geophys. Res. Lett.*, **35**, L17519, doi:10.1029/2008GL033666.
- Lui, A. T. Y. (1991), A synthesis of magnetospheric substorm models, *J. Geophys. Res.*, **96**(A2), 1849–1856.
- Lui, A. T. Y., et al. (2008), Determination of the substorm initiation region from a major conjunction interval of THEMIS satellites, *J. Geophys. Res.*, **113**, A00C04, doi:10.1029/2008JA013424.
- Lyons, L. R., et al. (2012), Auroral disturbances as a manifestation of interplay between large-scale and mesoscale structure of magnetosphere-ionosphere electrodynamic coupling, in *Auroral Phenomenology and Magnetospheric Processes*, *Geophys. Monogr. Ser.*, vol. 197, edited by A. Keiling et al., pp. 193–204, AGU, Washington, D. C., doi:10.1029/2011GM001152.
- Lysak, R. L., and W. Lotko (1996), On the dispersion relation for shear Alfvén waves, *J. Geophys. Res.*, **101**, 5085–5094.
- Marklund, G., T. Karlsson, and J. Clemmons (1997), On low-altitude particle acceleration and intense electric fields and their relationship to black aurora, *J. Geophys. Res.*, **102**, 17,509–17,522, doi:10.1029/97JA00334.
- Marklund, G. T., et al. (1998), Observations of the electric field fine structure associated with the westward traveling surge and large-scale auroral spirals, *J. Geophys. Res.*, **103**, 4125–4144, doi:10.1029/97JA00558.
- Marklund, G. T., et al. (2001), Temporal evolution of the electric field accelerating electrons away from the auroral ionosphere, *Nature*, **414**, 724–727.
- Marklund, G. T., S. Sadeghi, T. Karlsson, P.-A. Lindqvist, H. Nilsson, C. Forsyth, A. Fazakerley, E. A. Lucek, and J. Pickett (2011a), Altitude distribution of the auroral acceleration potential determined from Cluster satellite data at different heights, *Phys. Rev. Lett.*, **106**, 55002, doi:10.1103/PhysRevLett.106.055002.
- Marklund, G. T., et al. (2011b), Evolution in space and time of the quasi-static acceleration potential of inverted-V aurora and its interaction with Alfvénic boundary processes, *J. Geophys. Res.*, **116**, A00K13, doi:10.1029/2011JA016537.
- Marklund, G. T., et al. (2012), Cluster multipoint study of the acceleration potential pattern and electrodynamics of an auroral surge and its associated horn arc, *J. Geophys. Res.*, **117**, A10223, doi:10.1029/2012JA018046.
- Marklund, G. T., et al. (2004), Characteristics of quasi-static potential structures observed in the auroral return current region by Cluster, *Nonlinear Process. Geophys.*, **11**, 709–720.
- Maynard, N. C., W. J. Burke, E. M. Basinska, G. M. Erickson, W. J. Hughes, H. J. Singer, A. G. Yahnin, D. A. Hardy, and F. S. Mozer (1996a), Dynamics of the inner magnetosphere near times of substorm onsets, *J. Geophys. Res.*, **101**(A4), 7705–7736.
- Maynard, N. C., W. J. Burke, G. M. Erickson, E. M. Basinska, and A. G. Yahnin (1996b), Magnetosphere-ionosphere coupling during substorm onset, in *Third International Conference on Substorms (ICS-3)*, pp. 301–305, ESA SP389, Eur. Space Agency Spec. Publ., Noordwijk, Netherlands.
- McFadden, J. P., C. W. Carlson, and R. E. Ergun (1999), Microstructure of the auroral acceleration region as observed by FAST, *J. Geophys. Res.*, **104**, 14,453–14,480.
- Mende, S. B., H. U. Frey, V. Angelopoulos, and Y. Nishimura (2011), Substorm triggering by poleward boundary intensifications and related equatorward propagation, *J. Geophys. Res.*, **116**, A00I31, doi:10.1029/2010JA015733.
- Mende, S. B., et al. (2000), Far ultraviolet imaging from the IMAGE spacecraft, *Space Sci. Rev.*, **91**, 243–318.
- Morioka, A., Y. Miyoshi, F. Tsuchiya, H. Misawa, K. Yumoto, G. K. Parks, R. R. Anderson, J. D. Menietti, and F. Honary (2009), Vertical evolution of auroral acceleration at substorm onset, *Ann. Geophys.*, **27**, 525–535, doi:10.5194/angeo-27-525-2009.

- Morioka, A., et al. (2010), Two-step evolution of auroral acceleration at substorm onset, *J. Geophys. Res.*, *115*, A11213, doi:10.1029/2010JA015361.
- Mozer, F. S., and A. Hull (2001), Origin and geometry of upward parallel electric fields in the auroral acceleration region, *J. Geophys. Res.*, *106*(A4), 5763–5778.
- Mozer, F. S., C. A. Cattell, M. K. Hudson, R. L. Lysak, M. Temerin, and R. B. Torbert (1980), Satellite measurements and theories of low altitude auroral particle acceleration, *Space Sci. Rev.*, *27*, 155–213.
- Murphy, K. R., I. R. Mann, I. J. Rae, C. L. Waters, H. U. Frey, A. Kale, H. J. Singer, B. J. Anderson, and H. Korth (2013), The detailed spatial structure of field-aligned currents comprising the substorm current wedge, *J. Geophys. Res. Space Physics*, *118*, 7714–7727, doi:10.1002/2013JA018979.
- Murphy, K. R., I. R. Mann, I. J. Rae, A. P. Walsh, and H. U. Frey (2014), Inner magnetospheric onset preceding reconnection and tail dynamics during substorms: Can substorms initiate in two different regions?, *J. Geophys. Res.*, *119*, 9684–9701, doi:10.1002/2014JA019795.
- Nishimura, Y., L. Lyons, S. Zou, V. Angelopoulos, and S. Mende (2010), Substorm triggering by new plasma intrusion: THEMIS all-sky imager observations, *J. Geophys. Res.*, *115*, A07222, doi:10.1029/2009JA015166.
- Paschmann, G., S. Haaland, and R. Treumann (Eds.) (2003), *Auroral Plasma Physics*, ISSI, Kluwer Acad., Dordrecht, Netherlands.
- Rae, I. J., et al. (2009), Near-Earth initiation of a terrestrial substorm, *J. Geophys. Res.*, *114*, A07220, doi:10.1029/2008JA013771.
- Rae, I. J., C. E. J. Watt, I. R. Mann, K. R. Murphy, J. C. Samsom, K. Kabin, and V. Angelopoulos (2010), Optical characterization of the growth and spatial structure of a substorm onset arc, *J. Geophys. Res.*, *115*, A10222, doi:10.1029/2010JA015376.
- Rème, H., et al. (1997), The Cluster Ion Spectrometry (CIS) experiment, *Space Sci. Rev.*, *79*, 303–350.
- Roux, A., et al. (1991), Plasma sheet instability related to the westward traveling surge, *J. Geophys. Res.*, *96*, 17,697–17,714.
- Shiokawa, K. W., K. W. Baumjohann, and G. Haerendel (1997), Braking of high-speed flow in the near-Earth tail, *Geophys. Res. Lett.*, *24*, 1179–1182.
- Wygant, J. R., et al. (2000), Polar spacecraft based comparisons of intense electric fields and Poynting flux near and within the plasma sheet-tail lobe boundary to UVI images: An energy source for the aurora, *J. Geophys. Res.*, *105*, 18,675–18,692.
- Wygant, J. R., et al. (2002), Evidence for kinetic Alfvén waves and parallel electron energization at 4–6 R_E altitudes in the plasma sheet boundary layer, *J. Geophys. Res.*, *107*, 1201, doi:10.1029/2001JA900113.
- Zesta, E., E. Donovan, L. R. Lyons, G. Enno, J. S. Murphree, and L. Cogger (2002), Two-dimensional structure of auroral poleward boundary intensifications, *J. Geophys. Res.*, *107*(A11), 1350, doi:10.1029/2001JA000260.